Chapter 3

The Magnetosheath

E. A. Lucek[1], D. Constantinescu[2], M. L. Goldstein[3], J. Pickett[4], J. L. Pinçon[5], F. Sahraoui[6], R. A. Treumann[7], and S. N. Walker[8]

3.1 Introduction

3.1.1 Average magnetosheath properties

The magnetosheath lies between the bow shock and the magnetopause and is formed mainly from decelerated and deflected solar wind, with a small contribution of plasma from the magnetosphere. The observed magnetosheath plasma parameters show both large scale spatial ordering, imposed by the shape of the magnetopause, and variability dependent on the solar wind input. Because the nature of the bow shock depends on the orientation of the interplanetary magnetic field with respect to the local bow shock normal (θ_{Bn}), the properties of the magnetosheath plasma just behind the bow shock depend also on whether the shock is quasi-perpendicular or quasi-parallel. In general, the magnetosheath tends to be in a more turbulent state

[1]Space and Atmospheric Physics, The Blackett Laboratory, Imperial College London, London, UK
[2]Institut für Geophysik und extraterrestrische Physik, Technische Universität, Braunschweig, Germany
[3]NASA Goddard Space Flight Center, Greenbelt, MD, USA
[4]Department of Physics and Astronomy, The University of Iowa, Iowa City, IA, USA
[5]LPCE/CNRS, Orléans, France
[6]CETP/IPSL, Vélizy, France
[7]Max-Planck-Institut für extraterrestrische Physik, Garching, Germany
[8]Automatic Control and Systems Engineering, University of Sheffield, Sheffield, UK

Space Science Reviews 118: 95–152, 2005.
DOI: 10.1007/s11214-005-3825-2

behind the spatially extended quasi-parallel bow shock than it is behind the quasi-perpendicular shock. Lastly the plasma properties of the magnetosheath depend on properties of the upstream solar wind, including density, velocity and β.

The average properties of the magnetosheath have been documented based on data from several missions including ISEE 1 and 2 (e.g., Kivelson and Russell, 1995), AMPTE-IRM (Phan et al., 1994; Hill et al., 1995; Li et al., 1995), and Wind (Phan et al., 1996, 1997). Magnetosheath plasma is characterised by the following: first, its average density and magnetic field strength are higher than in the upstream solar wind by a factor consistent on average with the Rankin-Hugoniot relation for the fast mode shock; second, the average flow direction deviates from the anti-solar direction such that the plasma flows around the blunt magnetosphere; third, the velocity downstream of the bow shock is lower than the local fast magnetosonic speed; fourth, the flow velocity increases again to supersonic speeds around the magnetopause flanks; fifth, the ion temperature of the sheath is higher than in the solar wind while the electron temperature does not increase very much over its upstream value, such that the ion to electron temperature ratio in the sheath is of order $6-7$; sixth, the plasma β shows large variations from the order of unity to values much greater than one; seventh, the magnetosheath plasma develops a pronounced temperature anisotropy ($T_\perp > T_\parallel$) behind the bow shock that increases toward the magnetopause and is more pronounced in the ions than in the electrons. As a consequence of this the magnetosheath seems to develop two regions of different turbulent behaviour: one behind the bow shock and the other closer to the magnetopause.

3.1.2 Sources of low frequency waves and turbulence

As in the foreshock, there are multiple sources of waves and turbulence in the magnetosheath, but the physics of the latter is more difficult to untangle since the low frequency magnetic field fluctuations can be of order of $\langle \delta B^2 \rangle / B_0^2 \sim \mathrm{O}(1)$, which is in the strong turbulence regime. Embedded in the magnetosheath plasma are fluctuations arising from intrinsic solar wind turbulence, investigated extensively in previous work (Goldstein et al., 1995; Horbury et al., 1995; Horbury and Balogh, 1997; Marsch and Tu, 1997; Matthaeus et al., 1990; Roberts and Goldstein, 1991; Tu and Marsch, 1995), that have been processed as the plasma passed through the bow shock. Other fluctuations come from the foreshock region, where they are generated by reflected particle components (e.g., Paschmann et al., 1980, 1981). These waves have group velocities slower than the undisturbed solar wind speed and are therefore convected with the solar wind toward the shock front and into the magnetosheath. Further magnetosheath fluctuations are generated at the bow shock itself (e.g., Sckopke et al., 1983, 1990; Brinca et al., 1990).

As the magnetosheath plasma convects from the bow shock to the magnetopause the pressure anisotropy increases, and the free energy in the anisotropy can drive plasma instabilities (Crooker and Siscoe, 1977). The sense of the anisotropy, $p_\perp / p_\parallel >$

1, is opposite to that which leads to the excitation of the Alfvénic firehose mode. Instead, in a bi-Maxwellian plasma such an anisotropy can drive two instabilities which generate waves with frequencies below the ion cyclotron frequency. The first of these, the ion cyclotron instability, dominates when the temperature anisotropy is high and the proton plasma $\beta \sim 1$ and generates transverse electromagnetic ion cyclotron waves through a resonant wave particle interaction (e.g., Schwartz et al., 1996). Ion cyclotron waves typically have phase velocities close to the Alfvén speed and propagate away from their source region. The second, the mirror instability, tends to dominate under conditions of moderate temperature anisotropy and high plasma β (e.g., Schwartz et al., 1996). It generates large amplitude, anti-correlated variations in the magnetic field magnitude and plasma density which are non-propagating in the plasma frame. These structures can act as magnetic bottles, trapping part of the particle distribution (e.g., Kivelson and Southwood, 1996). For example, 'lion roar' oscillations are thought to be generated by anisotropic electrons trapped inside mirror structures (Baumjohann et al., 1999). Since mirror modes structures can be of large amplitude, introducing excess energy into the spectrum over a finite frequency band, it has been suggested that they could lead to both a forward and inverse cascade of energy to larger and smaller wavenumbers (e.g., Pokhotelov et al., 2003).

3.1.3 Cluster achievements

As described in the previous two sections, the magnetosheath is inherently complex. It is rich in waves and turbulence, and its properties are strongly influenced by processes occurring at, and upstream of, the bow shock. Since the properties of the bow shock vary in both space and time, so does the magnetosheath. Untangling the physics here, to understand wave generation, properties of the turbulence, and the evolution of the plasma behind the bow shock is therefore a challenge.

Previous studies have been limited by having measurements from only single or dual spacecraft missions. There was insufficient information to be able to uniquely identify wave modes, and it was very difficult to separate signatures of time evolution from those of spatial variation. For the first time, using the four point Cluster data, significant progress has been made in both of these areas, each essential for understanding how the magnetosheath works, and already new discoveries have been made. In addition, the polar Cluster orbit, which crosses the magnetosheath at high latitudes near noon and at the equator far on the flanks, samples regions which have not, until now, been comprehensively studied using such a sophisticated payload.

In the following sections we present some of the new results discovered using data from the Cluster mission. The following is a brief outline of the chapter:

- In section 3.2 two methods are presented which allow the unique identification of low-frequency wave modes present in the plasma. The methods are shown to

be complementary. One, *k*-filtering, allows the identification of multiple wave modes simultaneously supported by the plasma. It is found that, at frequencies below the ion gyro-frequency, these waves lie on MHD dispersion curves. The second, the phase difference method, allows the time variation of the dominant wave mode to be analysed on a time scale of only 15 seconds.

- In section 3.3 a study is presented of the low-frequency waves generated by particle temperature anisotropies downstream of the quasi-perpendicular bow shock, where they are for the first time unambiguously identified as Alfvén waves. These are then shown to evolve into field aligned current tubes, and it is suggested that this occurs under the action of the filamentation instability.

- Section 3.4 describes the derivation of a model of the 3D properties of local inhomogeneities introduced by the presence of mirror modes. This model is then compared with Cluster multi-point measurements, allowing an estimation of the mirror mode scale to be made.

- Section 3.5 describes the first statistical study of the occurrence and distribution of high frequency waves in the magnetosheath, including lion roars and a range of isolated electrostatic structures (IES). The observations suggest that magnetosheath IES might be being generated by a different mechanism, as yet unexplained, to that generating the IES seen in other regions.

- In Section 3.6 a type of dispersed ion signature found in the magnetosheath is described. The characteristics of these 'magnetosheath dispersed ion signatures' (MDSs) are used to develop a model which describes their generation by particle acceleration in a non-linear interaction between a solar wind discontinuity and the bow shock.

- Section 3.7 provides a summary and outlook.

3.2 Low Frequency Wave Mode Identification

3.2.1 Introduction

One major topic of study using Cluster data from the magnetosheath, has been the analysis of low frequency (LF) fluctuations, at frequencies below the ion gyrofrequency, where the new multi-spacecraft methods allow detailed analysis of the wave modes never previously possible with data from one or two spacecraft. The tetrahedron scale size relative to the wave vector is of particular importance in studying the magnetosheath wave field since many multi-spacecraft wave analysis methods require that the four satellites sample the same wave.

Many experimental studies of waves in the magnetosheath have focused on identifying linear modes at frequencies below the proton gyro-frequency, f_{ci}, (Anderson et al., 1994; Denton et al., 1994; Lacombe et al., 1995; Song et al., 1994;

Lucek et al., 1999). Before the Cluster mission, experimental analysis of the magnetosheath typically suffered from the spatio-temporal ambiguity that characterises single-satellite measurements. At times, analyses also lacked simultaneous field and plasma data. Under such conditions, wave mode identification was based on analysis of the relationship between the different components of the electromagnetic field and the plasma characteristics. Such methods were generally applied to 'wave-like' fluctuations, when the magnetic field power spectrum contained a clear peak, rather than to broadband fluctuations with power-law spectra. Typically these studies reported observations of Alfvénic fluctuations or ion cyclotron waves when the transverse magnetic field components were dominant, and mirror mode or slow waves when the fluctuations were compressional (e.g., Song and Russell, 1992). Moreover, the nature of the identified linear waves was found to depend on the depth in the magnetosheath, the geometry of the shock, β, the ion temperature anisotropy $A_i = T_\perp/T_{||} - 1$ and the frequency range analysed. High β and small A_i (e.g., $\beta_{i||} \approx 2$ and $A_i \approx 0.4$) were found to be favourable to mirror modes, whereas low β and large A_i (e.g., $\beta_{i||} \approx 0.2$ and $A_i \approx 2$) favoured EMIC (Electromagnetic Ion Cyclotron) waves (Anderson et al., 1994).

With data from only a single satellite it appeared difficult to go beyond this set of well established results. Denton et al. (1995) described the difficulty found with some events in identifying any linear mode. They suggested that either multiple modes were present in the same frequency range, or that non linear effects made the linear analysis suspect at best.

In these previous studies the presence of a unique wave vector at each given frequency had to be assumed, with a direction determined, for instance using minimum variance analysis (MVA). This restriction to monochromatic plane waves (one $\mathbf{k}$ for one frequency), even when justified, can only provide information on the mode containing the bulk of the energy. No information is obtained about other weaker modes in the wave field, which, when present, can compromise further analysis, of the wave polarisation for example. No method which assumes the presence of a single wave vector can be applied when the wave field is more properly represented as a superposition of several plane waves (i.e., with several wave vectors) containing comparable energies. Lastly, an additional complication arises because the waves are sampled in the spacecraft frame as they are carried across the satellites by the flowing plasma, while the theoretical linear waves are derived in the plasma frame (Omidi et al., 1994; Song et al., 1994). In the case when the wave speed is much smaller than the plasma flow speed, then it can be assumed that the waves do not change significantly in the time they take to cross the spacecraft, i.e., Taylor's hypothesis is satisfied, and the time series can be converted into a spatial cut through the plasma by taking into account the Doppler effect of the plasma velocity on the waves. However, in the magnetosheath the characteristic wave speed can often be of the same order of magnitude as the flow velocity, and it is therefore not usually possible to assume that Taylor's hypothesis is satisfied.

Now, with four point Cluster data it becomes possible under many circumstances to remove this spatio-temporal ambiguity and explore the three-dimensional motion of the electromagnetic and particle structures. One of the first studies to analyse magnetosheath data using a multi spacecraft wave identification method was presented by Glassmeier et al. (2001). They used a technique called the 'wave telescope' (Motschmann et al., 1996, 1998), which is similar in formulation to the *k*-filtering method discussed later in this section. They chose an interval where a clear, quasi-monochromatic wave was observed in the magnetic field data. They were able to identify uniquely the **k**-vector of the wave, finding that it had a wavelength of $\simeq 12.5 \times 10^3$ km, and was propagating nearly parallel to the ambient magnetic field.

In the following sections one interval of magnetosheath data (February 18, 2002 at around 05:34 UT), containing turbulent ULF magnetic fluctuations commonly seen in the high β magnetosheath plasma, is analysed using two methods, which allow the **k**-vectors of magnetosheath waves to be calculated. The first study by Sahraoui et al. (2003) describes the application of the *k*-filtering technique to magnetosheath fluctuations. In this analysis the wave field was modelled as a linear superposition of monochromatic plane waves. The *k*-filtering method allows the identification of multiple wave vectors at a single frequency by the application of a series of filters applied to data from all four spacecraft (Pinçon and Motschmann, 1998; Pinçon and Lefeuvre, 1991). The derivation of the filters can be constrained by various physical criteria, and in this case the results were obtained from a set of filters which incorporated the condition that $\nabla \cdot \mathbf{B} = 0$. The second study, presented in Walker et al. (2004), describes the results of the phase difference method for the same interval and compares the two methods. The phase difference method (Balikhin and Gedalin, 1993) also represents the wave field as superposition of plane waves, but in addition it assumes the dominance of a single **k** vector at a given frequency. At each frequency the **k** vector is estimated from the phase delays in the Fourier components, calculated using data from each of the four spacecraft. Both studies reveal complex physics. Walker et al. (2004) concluded that there is good agreement between the two methods in their identification of the dominant mode in the data set. They also show, however, that at some frequencies there is significant power in modes other than the dominant one.

On February 18, 2002, Cluster was on an outbound trajectory, crossing the magnetopause into the magnetosheath at ∼04:59 UT. The tetrahedron was located close to (5.6, 4.6, 8.4) R_E GSE, about 0.8 R_E outside the model magnetopause of Roelof and Sibeck (1993). The inter-spacecraft separation varied between 94 and 104 km. For both studies the shape of the tetrahedron is important and it has been shown that the two geometrical factors characterising the three-dimensional configuration of the spacecraft: elongation E and planarity P, have to take values ≤ 0.4 for the 3D configuration to be appropriate for application of the methods (Robert et al., 1998). For this interval both P and E were small: 0.04 and 0.08, respectively.

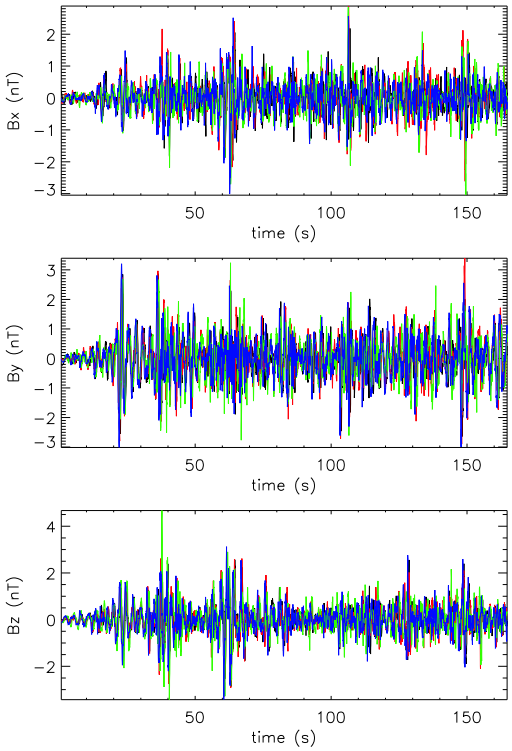

Figure 3.1. STAFF waveform data from February 18, 2002. The interval length is 164s, starting at 05:34:01.15 UT, and the data are high-pass filtered at the cut-off frequency $f_{cut-off} = 0.35$ Hz. From top to bottom the panels show the X, Y, and Z components of the magnetic field in the GSE frame. The coloured lines represent data from Cluster 1 (black), 2 (red), 3 (green), and 4 (blue). The waves in this interval were analysed using the *k*-filtering and phase difference methods. (From Sahraoui et al., 2003).

A comprehensive description of the magnetosheath plasma parameters for this interval derived from FGM, WHISPER and CIS can be found in Sahraoui et al. (2003). They used magnetic field data from both the STAFF search coil magnetometer (Cornilleau-Wehrlin et al., 1997) and FGM (Balogh et al., 2001) experiment, while Walker et al. (2004) used data from STAFF and from EFW (Gustafsson et al., 1997). The Cluster payload was operating in a telemetry mode, where STAFF and EFW were returning magnetic/electric field waveforms up to 10 Hz and sampled at 25 Hz. For both studies, the STAFF data were filtered using a high-pass filter with a cut-off frequency f_{co}=0.35 Hz. The purpose of this filter is to prevent any problems with the spacecraft spin, which might pollute the magnetic data at frequencies close to 0.25 Hz.

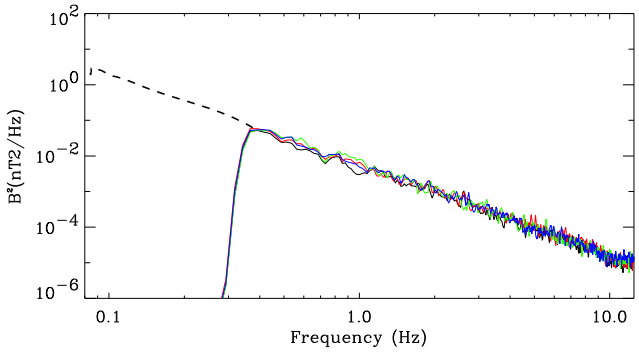

Figure 3.2. Power spectrum of the ULF magnetic fluctuations shown in Figure 3.1. This is close to a power-law $f^{-\alpha}$ with $\alpha \approx 2.2$. The coloured lines represent data from Cluster 1 (black), 2 (red), 3 (green), and 4 (blue). From Sahraoui et al. (2003).

3.2.2 Magnetic wave field energy distribution from *k*-filtering

The interval on February 18, 2002 selected for analysis by the *k*-filtering method was of length $\Delta T = 164\,s$, starting at 05:34:01.15 UT (see Figure 3.1). The modulus of the amplitude of the filtered magnetic fluctuations, normalised to the background magnetic field, was weaker than 15%, implying that the fluctuations in this interval can be interpreted using concepts from weak turbulence theory.

The power spectrum of the magnetic fluctuations in the frequency range 0.35 Hz to 12.5 Hz is shown in Figure 3.2. The spectral slope of the power-law fitted to this spectrum was ~ 2.2, and the spectrum was interpreted by the authors as being similar to those characterising the cascade of energy from large to small scales in turbulence theory. The spectra of the parallel and perpendicular components of the magnetic fluctuations (with respect to the background magnetic field) were compared to that of the sum of the component spectra, and it was found that both components looked similar.

Four frequencies were arbitrarily selected from the continuous spectrum between the low frequency cut off at $f_1 = 0.37$ Hz, and the maximum frequency which can be analysed accurately using the *k*-filtering technique, $\simeq 2$ Hz. The chosen four frequencies were: $f_1 = 0.37$ Hz, $f_2 = 0.49$ Hz, $f_3 = 0.61$ Hz, and $f_4 = 1.15$ Hz, and the *k*-filtering technique was applied. Here the results for $f = 0.61$ Hz are reviewed. Application of the *k*-filtering technique to the magnetic field data allows a comparison to be made between the distribution of the most significant portion of the magnetic field energy in the $(\omega, \mathbf{k})$ domain and the theoretical dispersion relation for propagating waves. For this purpose, it is convenient to display the data using magnetic field aligned (MFA) coordinates. In this coordinate system the *z*-axis is along the mean magnetic field $\mathbf{B}_o = B_o\mathbf{z}$, the x-axis is perpendicular to

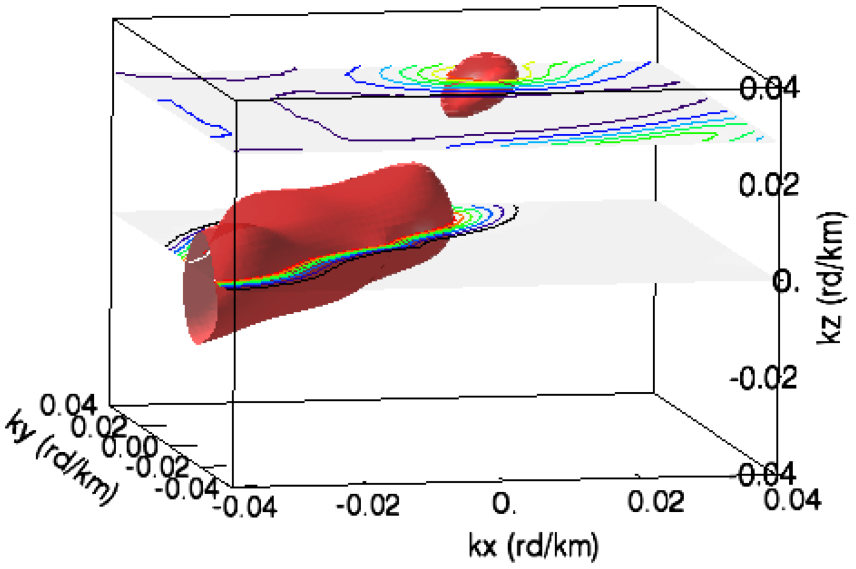

Figure 3.3. Three-dimensional display of the magnetic field energy distribution (MFED) in (k_x, k_y, k_z) space for $f = 0.61$ Hz showing the MFED isosurface corresponding to 33% of the MFED maximum value in the validity domain. Most of the energy is confined to two limited areas. Energy isocontours are drawn in the (k_x, k_y) plane for $k_z = -0.0007$ rad km^{-1} and $k_z = 0.0305$ rad km^{-1} with k_x and k_y values being (-0.04, 0.04) rad km^{-1} respectively. Figure 3.4 shows these two energy contribution plots. (Figure provided by J.-L. Pinçon.)

z-axis, in the plane containing the Sun-satellite line and the z-axis, and directed towards the Sun, and the y-axis completes the right-handed set.

A representation of the magnetic field energy distribution (MFED) at 0.61 Hz in the (k_x, k_y, k_z) domain is shown in Figure 3.3. The three-dimensional view was obtained by displaying the MFED isosurface corresponding to 33% of the maximum value. In this interval the most significant part of the field energy was confined to two distinct areas in (k_x, k_y): one plane at $k_z = -0.0007$ rad km^{-1} and the other at $k_z = 0.0305$ rad km^{-1}. Each (k_x, k_y) plane is restricted to the validity domain defined by $k_x, k_y \in [-0.04; 0.04]$ rad km^{-1}. The validity domain in the wave vector space is determined by the Cluster tetrahedron scale: to avoid aliasing, all the wavelengths have to be larger than the satellite separations, which are of the order of 100 km in the present case. The resolution in k-space along k_x, k_y, k_z was found to be sufficient to determine the MFED without loss of information about its three-dimensional shape.

Since the chosen frequency, $f = 0.61$ Hz, was of the same order as the local ion-gyro frequency, the MFED derived from k-filtering was compared to the lin-

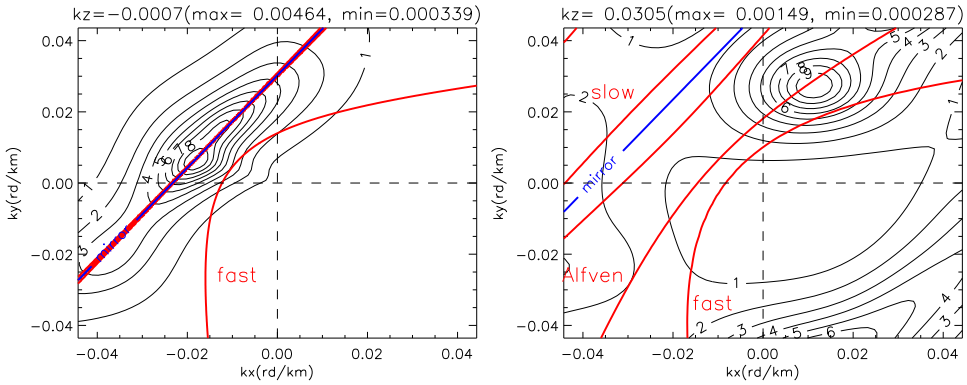

Figure 3.4. Two cuts through the magnetic wave field energy distribution (MFED), calculated for f = 0.61 Hz (as shown in Figure 3.3). The left panel is a cut at k_c = -0.0007 rad km^{-1} and the right panel at k_c = -0.0305 rad km^{-1}. Both panels show experimental magnetic energy (thin black lines) and the theoretical dispersion relations of the low frequency modes (coloured thick lines) as functions of k_x and k_y in the MFA frame. The blue line is the Doppler shift $\omega = \mathbf{k}.\mathbf{v}$. Two main peaks are identified: a mirror mode (left panel) and an Alfvén wave (right panel) having a frequency in the plasma frame close to the second gyroharmonic $f_{plasma} = 0.71\text{Hz} \sim 2f_{ci}$. (From Walker et al., 2004).

ear dispersion relations for the low frequency modes: mirror, Alfvén, fast and slow magnetosonic modes. These were derived from the WHAMP program (Rönnmark, 1983), using the plasma parameters applicable to this event. The mirror mode can be added by considering it as a non propagating mode $\omega_{mirror} = 0$ in the plasma frame. The MFED was computed in the MFA frame (which is at rest with respect to the satellite). Because the theoretical dispersion relations are obtained in the plasma frame, the influence of the Doppler effect was taken into account before the comparison was made. The relative velocity between the plasma and the spacecraft frames was derived from CIS data (Rème et al., 2001): $(V_x, V_y, V_z) \approx (-180, -130, -30)$ km s^{-1}in the MFA frame. The Doppler shift was estimated for each *k*-value and used to obtain the theoretical dispersion relations of the LF modes in MFA frame. The *k*-filtering results were then compared with the linear model of propagating waves.

Figure 3.4 shows a superposition of the theoretical LF dispersion relation (thick coloured lines) with isocontours of the MFED at the frequency $f = 0.61$ Hz. The results are presented for the two (k_x, k_y) planes corresponding to significant MFED maxima ($k_z = -0.0007$rad km^{-1} and $k_z = 0.0305$ rad km^{-1}) identified in Figure 3.4. The presence of both a mirror mode (left panel) and an Alfvén wave (right panel) is apparent. For a given frequency and k_z value, a mode is clearly identified when its theoretical curve in the (k_x, k_y) plane lies close to an observed magnetic energy peak. It should be noted that the superposition of the slow, Alfvén, and mirror dispersion curves in Figure 3.4 (left panel) reflects the degeneracy of these

modes at low frequencies in the plasma frame (≈ 0 Hz), particularly for this quasi-perpendicular direction of propagation ($\approx 87^\circ$ with respect to the local magnetic field). Such coexistence of several waves for a given frequency is not exceptional. Using the selected STAFF data the same *k*-filtering analysis was performed for three more frequencies in the range 0.35 Hz to 1.4 Hz and for each case the *k*-filtering technique showed the presence of several modes at a single frequency.

3.2.2.1 Discussion of the k-filtering analysis

By using the *k*-filtering technique to four point magnetic field data, Sahraoui et al. (2003) determined the magnetic field energy distribution in (k_x, k_y, k_z) space for four different frequencies, of which the results for $f = 0.61$ Hz have been presented here. In each case the energy observed at a single frequency could be attributed to the superposition of more than one wave. The experimental results were compared with a model of low frequency waves. The distribution of maxima in the MFED, in the wave vector domain was found to be consistent with the dispersion relations of ULF wave modes. The mirror mode was confirmed to be the dominant mode in the high β plasma analysed in this case, Doppler shifted to non zero frequencies in the MFA frame, but Alfvén and slow modes were also identified. The imaginary parts of the theoretical solution obtained from the WHAMP model were non-zero, suggesting that weak non-linear interaction between low frequency modes might counteract the effects of linear kinetic damping. There are further arguments in support of the validity of a model of weak turbulence for studying the coupling between large and small scale magnetosheath fluctuations. Not only was the amplitude of the magnetic fluctuations less than 15% of the background magnetic field, as already mentioned earlier, but the observed magnetosheath magnetic energy was distributed over several eigenmodes close to the theoretical ULF mirror, Alfvén, and slow modes.

Similar results were obtained when the analysis was repeated for an interval 25 minutes later, when Cluster was still in the magnetosheath, but to construct a global view of the magnetic fluctuations in the magnetosheath, similar studies are needed of low beta magnetosheath plasma, for which it is expected that other waves than the mirror mode might be dominant.

The next section will present the results from a comparison between the wave vectors resulting from the application of the *k*-filtering and phase differencing methods.

3.2.3 Application of the phase difference method

Use of synchronous data from two closely separated satellites allows the determination of wave modes as well as the direction of wave propagation. This has been done by applying either spectral/coherency analysis methods together with time delay information to the components of the magnetic field (Gleaves and Southwood, 1991), magnetic and thermal pressures, and MVA (Song and Russell, 1992), or by

computing the phase difference of the waves measured at each satellite (Balikhin and Gedalin, 1993; Balikhin et al., 2003; Dudok de Wit et al., 1995). The latter method yields the projection of the wave vector along the satellite separation direction. In certain circumstances the complete wave vector (both in magnitude and direction) can be constructed subsequently by employing MVA to find the wave propagation direction (Means, 1972) with respect to the vector of satellite separation. However, the use of MVA imposes limitations: it can only be applied to magnetic field wave data, and the wave in question should be monochromatic and elliptically polarised.

The previous section presented the application of the *k*-filtering method to an interval of magnetosheath data in order to derive the **k** vectors present in the wave field. In this section results are presented from analysis by Walker et al. (2004) of the same data set using the phase difference method to identify the main wave mode. A comparison of the results of the two methods is then made.

The *k*-filtering method was applied to 164 seconds of data from February 18, 2002, starting at 05:34:01.15 UT. Walker et al. (2004) analysed the same interval, both in its entirety and also by dividing it into sub-intervals in order to examine the time variation of the waves. As described in section 3.2.1 the phase difference method was applied to magnetic field data from STAFF, and to electric field measurements from EFW. The STAFF data were high pass filtered to remove spacecraft spin effects, and then converted from spacecraft coordinates to GSE. The EFW instrument measures the two components of the electric field in the spacecraft spin plane. The data were despun to remove most of the effects of spacecraft-spin. Since the GSE latitude of the spin vector of all spacecraft is $\approx$ -84 $^\circ$, the satellite reference frame is very close to an inverted GSE frame. The spin axis geometry also implies that the electric field booms might traverse the spacecraft wake, causing interferences at frequencies twice or four times the spin frequency in the E_x component of the electric field. Due to operational reasons it was not possible to measure the electric field vector on spacecraft 1. Therefore although the phase difference method could not be used to determine the wave vector of oscillations observed in the electric field, data from the remaining satellites was used to check the projection of the wave vector onto the separation vectors of spacecraft 2, 3, and 4.

Figure 3.5 shows the waveform of the magnetic field measured by the STAFF search coil magnetometer during the period between 05:34:15 and 05:35:15 UT on February 18, 2002. This interval corresponds to approximately the first minute of the total period and was the portion of data used in the wave vector determination process using the phase difference method. This period was chosen because the nature of the waves remained relatively stable during this time, and the $\omega - k$ spectra, calculated from data within 15 s sub-intervals were fairly consistent from one interval to the next. During the rest of the period the $\omega - k$ spectra were less clean and more variable. This variability is addressed further in Section 3.2.4

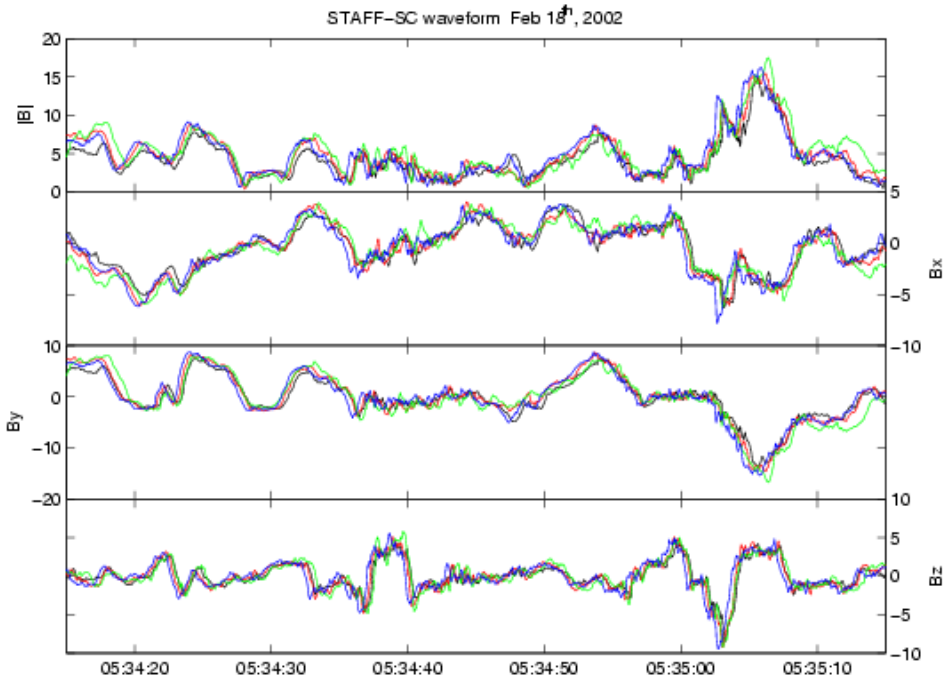

Figure 3.5. The magnetic field measured by the STAFF search coil between 05:34:15 and 05:35:15 UT on February 18, 2002. From top to bottom the panels show magnitude, and the X, Y, and Z components of the magnetic field in the GSE frame, all in nT. The coloured lines represent data from Cluster 1 (black), 2 (red), 3 (green), and 4 (blue). This interval corresponds approximately to the first minute of data shown in Figure 3.1. (From Walker et al., 2004).

The EFW waveforms are shown in Figure 3.6. The top panel gives the magnitude of the electric field measured in the spin plane of each satellite. The middle and bottom panels show the E_x and E_y spin plane components. The waveforms from satellites 3 and 4 are almost identical in nature. This is evident from the components of the electric field, in which fluctuations are observed first by Cluster 4 (blue) followed after a time delay of 0.4 seconds by Cluster 3. The waveforms show that the X component of the signal measured on satellites 3 and 4 was dominated by an oscillation with a period corresponding to half of the satellite spin period. The authors noted that the satellite spin signature was smaller in the Y component, and so analysis of this component was done for comparison with the results obtained from the STAFF search coil data.

Figure 3.7 shows the $\omega - k$ spectrum resulting from the analysis of satellite combinations (1,4), (2,4), and (3,4), calculated using data from STAFF for the time period 05:34:15-05:35:15 UT. A distinctive linear feature indicating an increase in

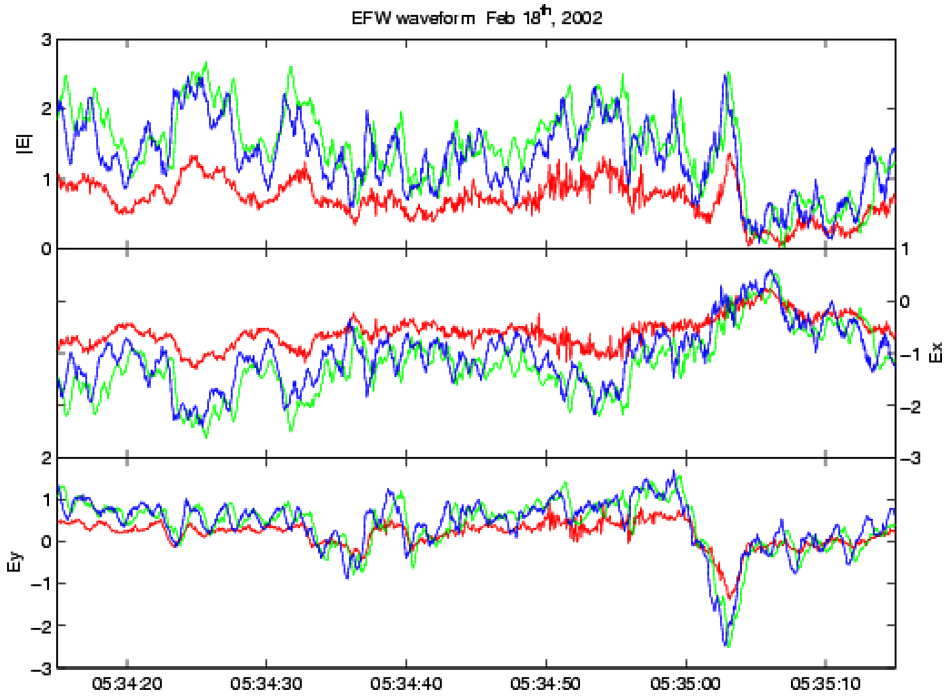

Figure 3.6. The electric field measured by the EFW instruments for the same interval as covered by Figure 3.5. From top to bottom the panels show the field magnitude, and the X and Y components in the spin plane. Units are in mV m^{-1}. The coloured lines represent data from Cluster 2 (red), 3 (green), and 4 (blue). The X component seen on satellites 3 and 4 shows fluctuations at twice the spin frequency that are probably the result of one of the probe pairs passing through the wake of the satellites. (From Walker et al., 2004).

phase difference with frequency is visible in all three cases. The positive gradient of these features implies that the waves were propagating from the second satellite in each of the pairings towards the first (for example from satellite 4 towards 1). A comparison of the dispersions calculated for all satellite combinations showed that the waves crossed the satellites in the order 4, 2, 3, 1. This result is generally in agreement with the crossing order observed in the waveform data shown in Figure 3.5, in which satellite 4 (indicated by the blue line) was always the first to observe any fluctuation in the field.

Due to the ambiguity in the determination of the phase difference, the $\omega - k$ spectra are periodic with period 2π. Thus in order to compute the value of $\mathbf{k}$ correctly it is important to determine the correct dispersion branch. The similarity of the STAFF-SC waveforms during this period implied that all satellites saw the same wave with time differences smaller than the inverse frequency. Therefore the cor-

rect branch to examine in the dispersion plot is the central one, i.e., the branch that converges to the point $f = 0\,\mathrm{Hz}$, $\Delta\psi/\mathbf{r} = 0$. This also implies that the wavelength of the waves being studied was much greater than the inter-spacecraft separation distance.

The white crosses in Figure 3.7 mark the peaks in the dispersion curve at frequencies of 0.37, 0.44, 0.62, and 1.1 Hz, corresponding approximately to those frequencies chosen by Sahraoui et al. (2003), as discussed in Section 3.2.2 The horizontal lines through the crosses represent the width of the peak in the dispersion at the frequencies studied. The **k** vector of the waves at each of these frequencies was determined and the results are shown in Table 3.1a. The typical error in the estimation of the projection of the wave vector along the satellite separation distance from the plots shown in Figure 3.7 is of the order of $\pm 1.7 \times 10^{-3}\,\mathrm{km}^{-1}$. This translates to an error of $\simeq 10^{\circ}$ in the determination of the direction of **k**. The direction of the **k**-vectors differed considerably from the minimum variance direction computed using the same data period, the difference being $\approx 40^{\circ}$. This is understandable since mirror modes have a linear polarisation and so the similarity between the intermediate and minimum eigenvalues implies that the minimum variance direction is not well defined.

Once the wave vector direction had been determined it was possible to identify the propagation mode of the waves. Using the Doppler equation the plasma frame frequency f_{plasma} was determined, shown in Table 3.1a. At the lower frequencies (0.37 and 0.44 Hz) the plasma frame frequency was close to zero whilst at higher frequencies the phase velocity of the waves V_{phase} was determined to be of the order $200\,\mathrm{km\,s}^{-1}$. The angle between the wave vector and the plasma bulk velocity was $\approx 25^{\circ}$ implying that the phase velocity of the wave was comparable with the projection of the plasma bulk velocity in the direction of the wave vector i.e., the wave was not propagating but was convected past the spacecraft in the plasma. Finally the angle of propagation with respect to the magnetic field was of the order of 85°. Walker et al. (2004) concluded from this evidence that the waves were likely to be mirror mode waves.

3.2.4 Comparison of *k*-filtering and phase difference results

For comparison with Table 3.1a, which shows the **k** vectors derived at four frequencies using the phase difference method, Table 3.1b shows the **k** vectors of the dominant wave mode identified using the *k*-filtering method, derived at nearly the same four satellite frame frequencies. As described in the previous section, the **k** vectors identified from the phase difference method were found to be propagating at an angle of 85° to the magnetic field, with plasma frame frequencies close to zero, consistent with the mirror mode. In addition, each of the dominant **k**-vectors found by the *k*-filtering method were approximately perpendicular to the background magnetic field ($\Theta_{Bk} \approx 87^{\circ}$). Once again, their corresponding frequencies in the plasma frame were almost zero and therefore these waves were also attributed

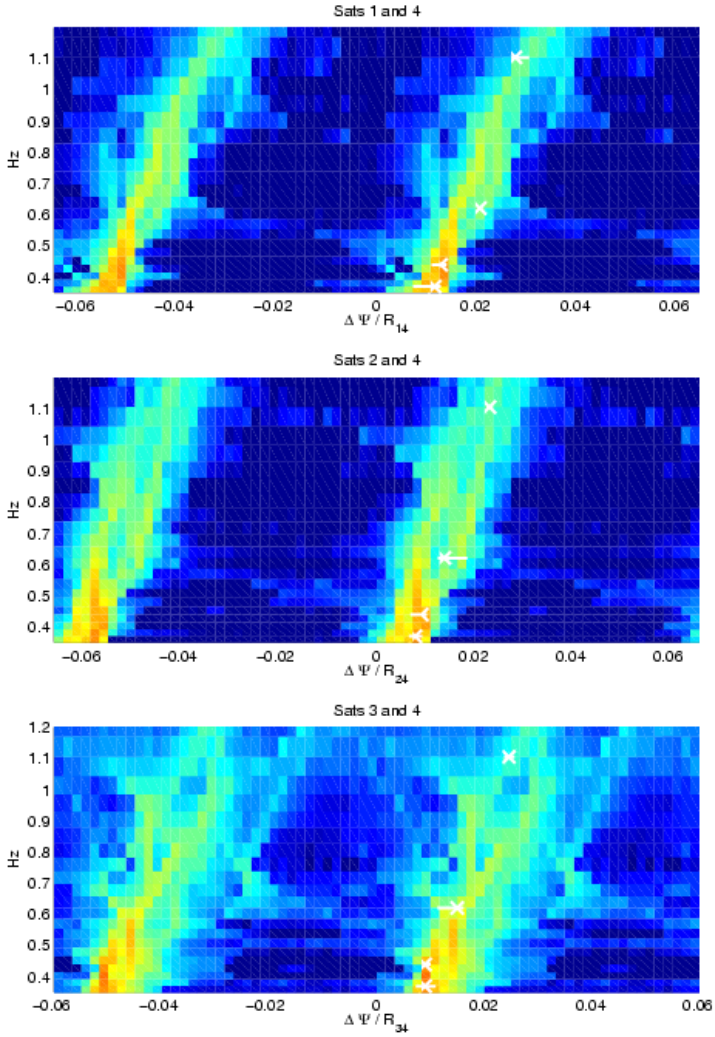

Figure 3.7. The $\omega - k$ joint spectrogram computed using STAFF search-coil data in the time period 05:34:15-05:35:15 UT for the satellite pairs (1,4), (2,4), and (3,4). The joint spectrogram is composed of a set of histograms, computed at a number of frequencies and stacked vertically. Each histogram shows the distribution of the observed phase differences between the two spacecraft, divided by the satellite separation distance, with the colour representing T the number of times a particular value was seen. The white crosses represent the phase differences ($\Delta\Psi/R_{xy}$) at the frequencies used in both the phase differencing and *k*-filtering analysis methods. (From Walker et al., 2004).

to the mirror mode. A comparison, therefore, of the results from the phase difference and *k*-filtering techniques shows that both methods identified the dominant fluctuation present in the data to be a mirror mode. The magnitudes of the **k** vectors

a) Wave vectors from phase difference method.

f_{sat} Hz	f_{plas} Hz	k_x rad km^{-1}	k_y rad km^{-1}	k_z rad km^{-1}	$\|\mathbf{k}\|$ rad km^{-1}
0.37	0.03	-0.009959	-0.003494	0.006239	0.0122
0.44	0.01	-0.009969	-0.00462	0.007797	0.01347
0.62	0.13	-0.016833	-0.006143	0.0119	0.02151
1.10	0.2	-0.0253	-0.01283	0.01264	0.03106

b) Wave vectors from **k**-filtering method.

f_{sat} Hz	k_x rad km^{-1}	k_y rad km^{-1}	k_z rad km^{-1}	$\|\mathbf{k}\|$ rad km^{-1}
0.37	-0.01097	-0.00236	0.00528	0.01241
0.44	-0.01241	-0.00279	0.00529	0.01378
0.61	-0.01671	-0.00404	0.00682	0.01849
1.12	-0.03065	-0.00941	0.01438	0.03514

Table 3.1. a) Wave vectors, **k**, computed for the four frequencies being investigated using the phase difference method. b) The computed characteristics of the most intense identified wave for the four studied frequencies using the *k*-filtering technique. (After Walker et al., 2004).

	Satellite pair		
	(1,4)	(2,4)	(3,4)
$\mathbf{k}_{\mathrm{STAFF}}$	-0.01087	-0.00739	0.00837
$\mathbf{k}_{\mathrm{EFW}}$	-	-0.0074	0.0084
$\mathbf{k}_{k-filt}$	-0.00943	-0.00556	0.01055

Table 3.2. Wave vectors, **k**, projected along the satellite separation vectors. The frequency used was 0.37 Hz. The values were determined using the phase based method with both STAFF-SC ($\mathbf{k}_{\mathrm{STAFF}}$), and the EFW electric field ($\mathbf{k}_{\mathrm{EFW}}$), and by applying the *k*-filtering method to the STAFF-SC ($\mathbf{k}_{k-filt}$) data set. (From Walker et al., 2004).

were comparable: for example at a frequency of 0.37 Hz $\omega - k$ dispersion yields $|\mathbf{k}| = 0.0122\,\mathrm{rad\,km^{-1}}$ versus the *k*-filtering results of $|\mathbf{k}| = 0.0124\,\mathrm{rad\,km^{-1}}$, while at a frequency of 0.44 Hz the magnitudes $|\mathbf{k}|$ are 0.0135 and 0.00138 rad km^{-1} for the phase difference and *k*-filtering methods, respectively. In the case of both frequencies the angles between the vectors was $\approx 8^{\circ}$ which is less than the error in the phase difference technique.

The **k**-vectors derived from the phase difference method were also compared with results obtained using the same method applied to EFW electric field data.

However, as noted earlier, electric field data were not available from spacecraft 1 so it was not possible to calculate the full wave vector **k**. It was, however, possible to calculate the projection of the wave vector along the satellite separation directions and hence to determine the value of the **k** vector projected onto the satellite separation directions (2,4), and (3,4). Table 3.2 lists the projections of the wave vector along the satellite separation directions used in the analysis and shows that the **k** directions determined using the phase difference method with STAFF-SC and EFW data gave identical results. Thus the authors concluded that they could be fairly confident of the values of **k** they found. In a similar way, a further comparison between the phase difference and *k*-filtering methods, was made by comparing the projection of those two wave vectors onto the spacecraft separation vectors. This is also shown in Table 3.2, where Walker et al. (2004) note that, at low frequencies, the values are comparable.

Comparison of the **k**-vectors from two methods at higher frequencies in Table 3.1 shows that the difference increases for higher frequencies. This is because at higher frequencies the error in the phase difference method can be larger because of the presence of other modes of comparable energies, seen by the fact that the *k*-filter method identified other wave modes as well as the mirror mode. Table 3.3 shows the properties of the weaker waves identified by the *k*-filtering technique at each of the four frequencies studied. These modes correspond to slow, Alfvén and ion cyclotron modes. An example of such a coexistence between several waves for one given frequency was shown in Figure 3.4. Both an Alfvén wave (left panel) as well as a mirror mode (right panel) were found to be present in the data.

f_{sat} Hz	$\lvert\mathbf{k}\rvert$ rad km^{-1}	$\theta \equiv (\mathbf{k}, \mathbf{B}_0)$	f_{plasma} Hz	Mode	I
0.37	0.01914	-30°	-0.14$\sim 0.4\, f_{ci}$	Slow	12%
0.44	0.02326	-45°	-0.29	Alfvén$\sim f_{ci}$	21%
0.61	0.04246	44°	0.71	Alfvén$\sim 2\, f_{ci}$	33%
1.12	0.04553	-57°	1.99	Cycl.$\sim 6\, f_{ci}$	98%

Table 3.3. Using the *k*-filtering technique other waves with lower intensities are identified for the four studied frequencies. Only the first secondary maxima are given here. In Column 'I' are given their intensities compared to that of the dominant wave for the corresponding frequency. f_{plasma} is the relative frequency in the plasma frame, $f_{ci} = 0.33$ Hz is the proton cyclotron frequency. (Reproduced from Walker et al., 2004).

The main result from this analysis was that up to a frequency ~ 0.7 Hz in the satellite frame, slow and Alfvén modes coexisted with the dominant mirror one. At higher frequencies, proton cyclotron harmonics were identified as having energies comparable to the mirror mode. The tendency of the mirror mode to lose its dominant character can be seen from column 'I' in Table 3.3 which shows the energy in

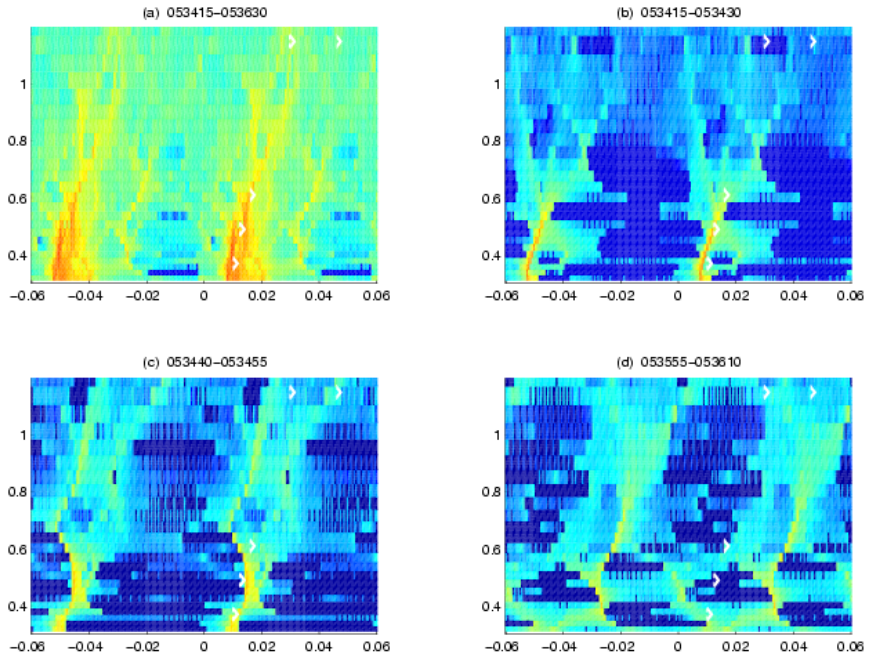

Figure 3.8. A set of snapshots of the $\omega - k$ dispersion. Panel (a) is calculated using data covering the full period 05:34:15-05:36:30 UT, in the same format as Figure 3.7. The other snapshots are computed using 15 s time intervals within the period under study. In all cases data from spacecraft 3 and 4 were used. Superimposed onto each plot, indicated by white symbols, are the mirror mode wave vectors determined from *k*-filtering, projected onto the satellite separation vectors. (From Walker et al., 2004).

the first secondary maximum as a percentage of the energy in the dominant mode. For $f = 1.12$ Hz the sixth cyclotron harmonic has comparable energy to that in the mirror mode.

The wave environment was highly variable on the time scale studied here. Figure 3.8 shows snapshots of the $\omega - k$ spectra, calculated using STAFF-SC data for the satellite pair (3,4), at different times within the time interval under investigation. Panel (a) shows the $\omega - k$ spectrum calculated for the whole period 05:34:00-05:36:44 UT. A number of different dispersion branches are visible. The main branch corresponds to the wave number range $0.01 < \Delta\psi/\mathbf{r}_{34} < 0.015$ at 0.35 Hz. At higher frequencies 0.4-0.5 Hz this branch exhibits a double peak in k-space and at the highest frequencies analysed it splits into two distinct branches. The projection of the mirror mode **k**-vectors determined from *k*-filtering are indicated with white symbols. For 0.35-0.8 Hz a second branch appears to the right of the main dispersion branch. It is of lower intensity and corresponds to a different mode.

The other three panels show results calculated from three intervals, each of 15 s duration, significantly shorter than the 1 minute interval used to generate the results shown in Figure 3.7. Panel (b) shows the $\omega - k$ spectrum calculated using data for a 15 s period starting at 05:34:15 UT. A well defined branch, corresponding to the mirror mode determined from *k*-filtering, appears below 0.7 Hz. The dispersion curves extend to higher frequencies but with lesser amplitudes. Panel (c) gives the $\omega - k$ spectrum for a 15 s snapshot starting near 05:34:40 UT. At low frequencies, the dispersion branch still resembles the mirror mode dispersion whilst at higher frequencies it splits into two sections, both of which were identified as mirror modes. Finally, panel (d) shows another 15 s snapshot towards the end of the investigated time interval, beginning at 05:35:55 UT. Now the mirror mode has disappeared completely and the branch lying to the right of the main branch identified in panel (a) becomes the dominant mode.

Walker et al. (2004) noted that by performing *k*-filtering on shorter time intervals it can be shown that the results change as a consequence of underestimating the energy contributed by various other modes, but that the determined wave vectors remain unaffected. They also describe the advantages and disadvantages of the two different methodologies used to identify wave modes. The phase difference method, implemented using a wavelet transform based on the Morlet wavelet, can be used to analyse a shorter period of data than the *k*-filtering technique, thus revealing time dependent behaviour of the plasma, while the Fourier transform in *k*-filtering enables the determination of the energy density in the individual wave modes, information not available from the Morlet wavelet transform used in the phase difference method. Also, the phase difference method works best when only one wave mode is present or when one wave mode dominates the wave environment, since multiple modes result in multiple dispersion curves rendering the wave vector directions unresolvable. Methods to resolve this problem are currently being pursued. Hence, the *k*-filtering technique can resolve the presence of multiple waves within the plasma, while the phase differencing technique can access the time dependence. Thus, in some sense, the two methods are complementary.

To summarise, two complementary methods were used to combine data from four spacecraft, during an interval when broadband waves were observed in the magnetosheath. The results demonstrate that during this time the plasma contained multiple wave vectors at each frequency studied. Furthermore, these wave modes were found to lie on MHD dispersion curves, allowing the identification of multiple MHD wave modes present simultaneously in the data. Thus, in this case, the broadband wave spectrum in the plasma was shown to arise from the superposition of linear MHD modes, leading to the conclusion that a weak turbulence approach is appropriate for understanding the plasma at this time.

3.3 Waves Behind the Quasi-Perpendicular Bow Shock

The structure of supercritical, quasi-perpendicular shocks is dependent on the motion of gyrating ions reflected from the shock ramp. The reflected ions pass downstream where they contribute to an ion temperature anisotropy such that $T_{i\perp} > T_{i\|}$. As described in Section 3.1.1, such an ion temperature anisotropy can drive either Alfvén ion cyclotron or mirror instabilities (e.g., Schwartz et al., 1996; Gary et al., 1994).

Alexandrova et al. (2004) presented an analysis of waves and small scale filamentary structures observed downstream of a quasi-perpendicular, super-critical bow shock. They found that the plasma conditions immediately downstream of the shock ramp were appropriate for the generation of electromagnetic Alfvén ion cyclotron waves (AIC) waves. Using data from the four spacecraft, the authors were able to demonstrate for the first time that the two quasi-monochromatic waves observed downstream of the shock had properties consistent with generation by proton and alpha cyclotron waves. Further downstream the AIC waves ceased abruptly. At the same time the temperature anisotropy decreased and signatures consistent with cylindrical current tubes aligned with the magnetic field were found. The authors concluded that the current tubes evolved downstream of the shock from the Alfvén waves under the action of the filamentation instability (Laveder et al., 2002) occurring where the total plasma $\beta > 1$.

3.3.1 Observations

Alexandrova et al. (2004) examined several crossings from March 31, 2001 previously studied by Maksimovic et al. (2003), presenting in detail the results from one crossing which occurred at 18:02:17 UT. Four-spacecraft timing discontinuity analysis was used to estimate a normal for the shock surface, **n**, which was then refined using the constraint that the observed direction of maximum magnetic field variance **b** should be orthogonal to the bow shock normal: $\mathbf{n} = -\mathbf{b} \times (\mathbf{b} \times \mathbf{n})$. This led to a small correction in the shock normal. The unit vectors **b** and **n** were then used to define the shock normal co-ordinate system. When the average upstream and downstream magnetic fields were estimated, their components in the shock normal direction were almost the same, supporting the shock normal estimation.

Data from the STAFF search coil experiment (Cornilleau-Wehrlin et al., 1997, 2003), high pass filtered to remove the spacecraft spin signal at 0.25 Hz, were combined with four second averaged magnetic field data from FGM (Balogh et al., 2001) using a Haar wavelet transform, in order to obtain a 'mixed' signal covering both low frequency variations and high frequency waves. This procedure is described in detail in Alexandrova et al. (2004). Using data from ACE (for the solar wind plasma parameters) and the instruments on Cluster, characteristic upstream and downstream plasma parameters were calculated, including average magnetic field (B), proton and alpha gyrofrequencies (f_{cp}, $f_{c\alpha}$), plasma flow velocity (V),

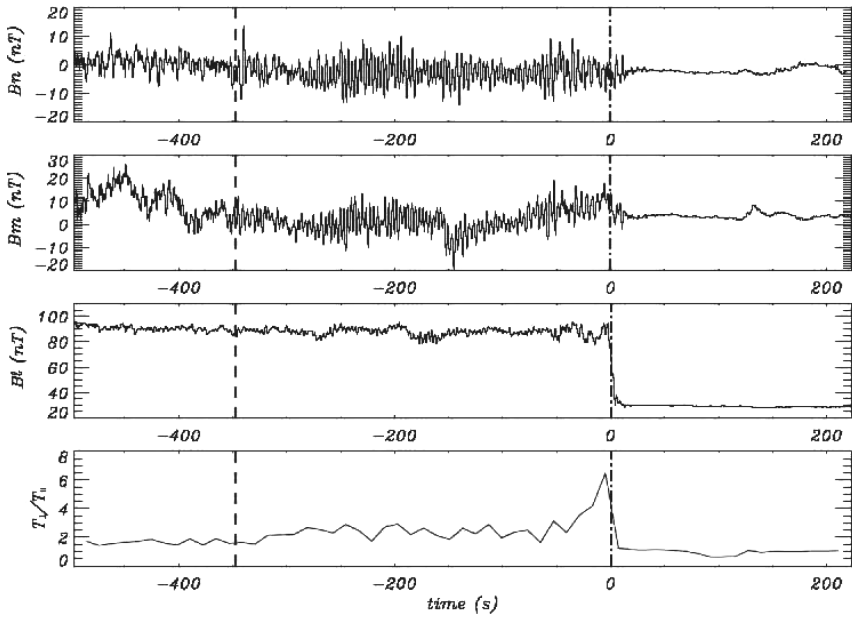

Figure 3.9. Combined magnetic profile from STAFF and FGM field data, from Cluster 1, between 17:54 and 18:06 UT on March 31, 2001 in shock normal co-ordinates: panel 1, B_n, the magnetic field component along the shock normal; panel 2, B_m, the magnetic field component in the direction perpendicular to the maximum variance and the shock normal directions; panel 3, B_l, the magnetic field component along the shock maximum variance direction; panel 4, the proton temperature anisotropy. The origin for time is taken at the shock crossing, at 18:02:17 UT (dash-dotted line), so that negative times correspond to data from the magnetosheath. The vertical dashed line, at 17:56:30 UT, marks the transition between two regions: the first contains signatures of current tubes and the second contains well developed, quasi-monochromatic, transverse wave activity. (From Alexandrova et al., 2004).

proton and electron temperatures (T_p, T_e), proton, alpha and electron densities (N_p, N_e, N_α), Alfvén velocity (V_A), ion inertial length (c/ω_{pi}), and ion and electron plasma beta (β_p, β_e). The shock was found to have a $\theta_{Bn} \sim 82^\circ$, and a Mach number $M_A \sim 4.4$, and was therefore both quasi-perpendicular and supercritical. In addition, the parallel electron and proton temperatures ($T_{e\|}$, $T_{p\|}$) and corresponding anisotropies ($T_{e\perp}/T_{e\|}$, $T_{p\perp}/T_{p\|}$) were estimated.

3.3.2 Alfvén ion cyclotron waves

Figure 3.9 shows the 'mixed' magnetic field data, obtained by combining STAFF and FGM data, for the shock and the downstream region. Immediately downstream of the shock, well developed transverse wave activity was observed for ~ 300 seconds. An analysis of the observed waves was made in the context of expectations from linear wave theory: using the background magnetosheath plasma parameters, and assuming bi-Maxwellian particle distributions for electrons, protons and alpha

particles, a linear model, WHAMP (Rönnmark, 1983), was used to calculate the most unstable modes. These were found to be Alfvén waves propagating parallel to the background magnetosheath magnetic field. Positive growths rates in two frequency bands were obtained: 0.24 f_{cp} and 0.51 f_{cp}, corresponding to wave modes excited by the alpha and proton temperature anisotropies respectively. The power in the lower frequency wave was found to be greater than that in the higher frequency. The authors represented these wave modes in terms of the normalised wave vector, kr_p, parallel to the magnetic field, where r_p is the proton Larmor radius based on the proton parallel thermal velocity $r_p = (2k_B T_{p\|})$. Described in this way the two unstable wave modes were centred on $k_1 r_p = 0.19$ and $k_2 r_p = 0.45$.

A power spectrum of the fluctuations observed by Cluster showed two peaks separated by approximately a factor of 2, at 0.29 and 0.57 Hz. The minimum variance direction during the wave activity was found to be within 10° of the average magnetosheath magnetic field, suggesting that the waves were nearly field aligned. The waves were also left-hand, nearly circularly polarised with respect to the background magnetic field. The wave vectors of the two waves were estimated by applying the four-spacecraft phase difference method to magnetic field data during the wave activity, using data from Cluster 1 as the reference set and solving

$$[\phi_1(f) - \phi_i(f)] = (\mathbf{k} \cdot \delta \mathbf{r}_{1i}) + 2\pi n_{1i}, \quad i = 2,3,4 \tag{3.1}$$

The 2π ambiguity was removed by constraining the solution such that (1) the solution was parallel to the minimum variance direction, (2) the angle between the wave vector and the background magnetic field was small, as expected from linear theory, (3) the sum of the differences in Equation 3.1 was minimised and (4) the value of n_{1i} in Equation 3.1 was the smallest value satisfying the constraints listed above. The following results were obtained for the two waves: $\mathbf{k}_1 = 14 \times 10^{-3}(0.27, -0.26, -0.93)$ km s^{-1}for the wave at $f_1 = 0.29$ Hz and $\mathbf{k}_2 = 25 \times 10^{-3}(-0.07, -0.23, -0.97)$km s^{-1}for the wave at $f_2 = 0.57$ Hz. The waves had unit vectors, expressed in shock normal co-ordinates, of $\mathbf{e}_1 = (0.08, 0.12, 0, 99)$ and $\mathbf{e}_2 = (-0.25, 0.18, 0, 95)$, which were approximately parallel (within $\sim 10°$ and $\sim 15°$ respectively) to the background magnetic field in the magnetosheath.

The properties of the observed transverse waves were compared with the expectations from linear Vlasov theory. The observed waves had plasma rest frame frequencies of $f_{0,1} = 0.43 f_{cp}$ and $f_{0,2} = 0.58 f_{cp}$, with normalised k vectors of $k_{1\|} r_p = 0.31$ and $k_{2\|} r_p = 0.55$. Therefore, although there was qualitative agreement between the observed and predicted waves, there was not exact correspondence. It was suggested that a better quantitative agreement might be achieved by having better defined background plasma parameters to use as input to the linear model. The authors concluded however that the observed wave frequencies, polarisation, dispersion characteristics and correspondence with linear theory were sufficient to positively identify the waves as Alfvén ion cyclotron waves, excited by proton and alpha anisotropies.

It was noted that, although the AIC waves were periodic, they were not sinusoidal. Instead they had steepened wave fronts, which the authors suggested was indicative of the presence of relatively strong non-linearities. A systematic analysis of the regions of steepened magnetic field profile was made. Regions of steep local gradient were defined by the energy density in the smallest scale of a Haar wavelet transform exceeding the average energy density at this scale by a threshold factor, ν. The identification of these regions was found to be independent of the value of ν, as long as it exceeded $3-5$. Analysis of 2 seconds of magnetic field data centred on each region of local steepening showed that their magnetic signatures were consistent with those of current sheets, lying approximately parallel to the AIC wave fronts, and the authors suggested that they were produced by non-linear steepening of the waves.

3.3.3 Filamentary current tubes

Well developed AIC waves were observed for about 350 seconds in the region downstream of the outbound quasi-perpendicular shock crossing. The plasma populated by these waves had a proton $\beta_p < 1$ and $T_{p\perp}/T_{p\|} > 1$ and the onset of the waves occurred simultaneously with an abrupt change in $T_{p\perp}/T_{p\|}$. Prior to the interval of transverse wave activity, i.e., further downstream of the shock, magnetic perturbations were identified which were interpreted as three-dimensional current tubes aligned with the background magnetosheath magnetic field. Transformation of the magnetic field data into local minimum variance co-ordinates showed a systematic variation of all three components, with the minimum variance direction approximately aligned with the background magnetic field.

The Cluster tetrahedron scale at this time was $\sim$600 km, and two spacecraft: Cluster 1 and Cluster 4, had a separation vector inclined at only $\sim 20^\circ$ to the magnetic field. Comparison of data from this spacecraft pair revealed a good correlation between the magnetic field signatures for two structures, confirming that the structures were field aligned. The authors concluded on this basis that the structures had a field parallel dimension in excess of 620 km. Using the time delay between the structures being seen at the spacecraft, together with the separation of the two satellites in the plane perpendicular to the average magnetic field, allowed the authors to estimate the speed of the structures perpendicular to **B**. They estimated a velocity of $\sim$ 140 km/s in this plane, with the uncertainty of 10° in the orientation of the structures with respect to **B** giving a range for the velocity of $70-230$ km. The upper limit of this range was close to the background plasma flow velocity.

The observed magnetic perturbation was compared with a simple 2-D model of a localised current tube. In the model the current tube was assumed to have a cylindrical shape, to be aligned with the magnetic field (which was in the **z** direction), and to have properties which were independent of distance along the tube axis. The model was characterised by two functions: the perturbation of the magnetic field component parallel to the tube axis ($\delta B_z(x,y)$), and the variation of the z compo-

nent of the vector potential ($\mathbf{A} = A\mathbf{e_z}$), both as functions of position in the (x,y) plane perpendicular the tube axis:

$$\delta B_z = \Delta B_{\|} \exp^{(-R^2/R_0^2)} \tag{3.2}$$

$$A = \left(\frac{\Delta B_{\perp}}{\Delta B_{\|}}\right) R_0 \delta B_z \tag{3.3}$$

where $\Delta B_{\perp}$ and $\Delta B_{\|}$ characterise the amplitude of the parallel and perpendicular magnetic field perturbations generated by the current tube, R_0 is the radius of the current tube and R is the distance from the tube axis. By assuming that the spacecraft crossed the tube in the (x,y) plane, the best fit between the model and the observations was obtained with $R_0 = 60$ km, $\Delta B_{\|} \sim 15$ nT, $\Delta B_{\perp}/\Delta B_{\|} \sim 2$ and $R = 30$ km. Figure 3.10 shows a comparison of the data and the model fit for one current tube signature observed by Cluster 1 at 17:55:16 UT. There is good agreement between the magnetic field components transverse to the inferred current tube axis ($\delta B'_x, \delta B'_y$) with some deviation for the axis aligned component ($\delta B'_z$), which has the smallest amplitude variation of the three.

Similar structures were also observed by Cluster 2 during this interval, but the inter-spacecraft separation between Cluster 2 and spacecrafts 1 and 4 were $\delta R_{\perp 12} = 650$km $\delta R_{\perp 24} = 720$km: in each case much larger than the estimated current tube diameter and so the authors concluded that they could not be certain that Cluster 2 was observing the same current structure. Magnetic field data measured by Cluster 3 during this time contained similar signatures, but there was a data gap at the time that this particular current tube might have been observed.

3.3.4 Conclusions

Alexandrova et al. (2004) analysed magnetic perturbations downstream of a supercritical quasi-perpendicular shock observed on March 31 2001 when the Cluster tetrahedron scale was ~ 600 km. Figure 3.11 illustrates the processes which they suggested occurred downstream of the shock in this case. The shock generated a region of high temperature anisotropy immediately downstream, which was unstable to the excitation of proton and alpha AIC waves. Using data from the four spacecraft, they were able to make the first accurate identification of AIC waves in this region by comparison of the wave properties with those expected from linear theory (Rönnmark, 1983). Good qualitative agreement was found, although there were some differences, perhaps arising from uncertainties in the background plasma parameters. The authors proposed that these waves then collapsed into field aligned current filaments, through the action of the filamentation instability (Laveder et al., 2002). They used dual spacecraft observations of the same structure to demonstrate that the current tubes had an extent along the magnetic field of more than 600 km. They then fitted the observations to a simple two-dimensional model of a field

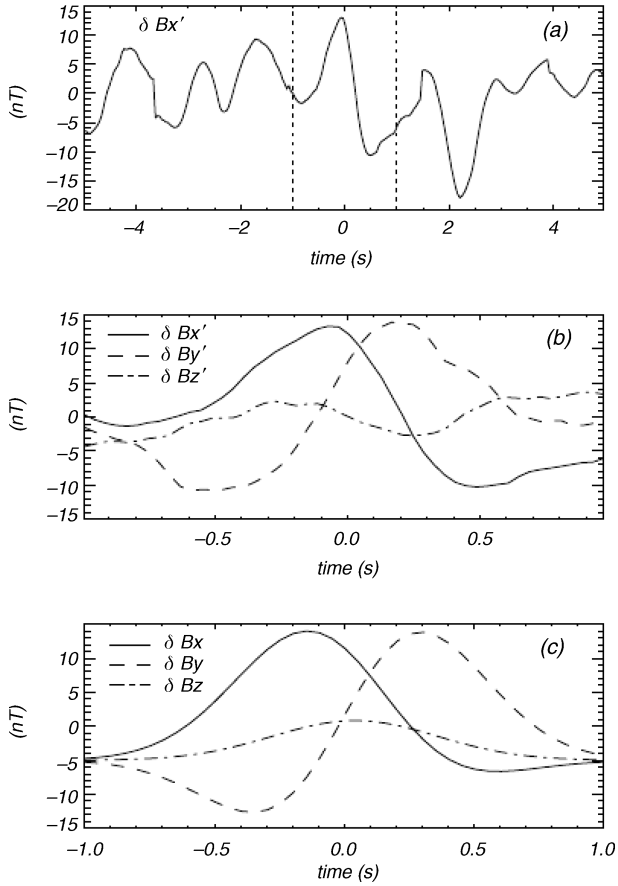

Figure 3.10. Magnetic field fluctuations plotted as a function of time, taking 17:55:16 UT as the time origin, in co-ordinates defined by MVA applied to the interval indicated by the vertical dashed lines in panel (a). In this co-ordinate system x' is in the maximum variance direction, and y' and z' in the intermediate and minimum variance directions respectively. Panel (a) shows 10 seconds of data of the B'_x magnetic field component, (b) shows the three components for a single current tube, for the time interval between the two dotted vertical lines in panel (a), and (c) shows the model data, where z is along the tube axis and x and y are in the plane perpendicular to the axis. There is good agreement for the components in the plane of the current tube perpendicular to its axis. (From Alexandrova et al., 2004).

aligned current tube, and estimated that the filaments had a radius of ~ 60 km: of the order of the local ion inertial length ($c/\omega_{pi} = 35$ km). The onset of the region populated by current filaments was associated with a decrease in the temperature anisotropy, which led the authors to suggest that the filamentation instability might play an important role in the relaxation of the plasma downstream of the shock.

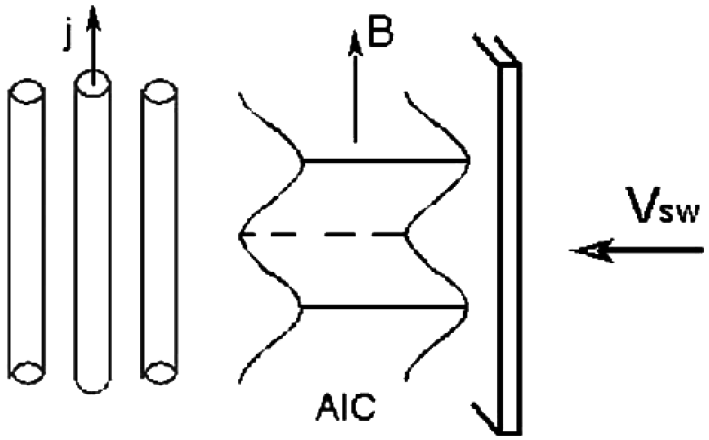

Figure 3.11. Schematic presentation of the generation and filamentation of AIC waves downstream of the perpendicular bow shock. The solar wind flows from the right into the shock (shown as a vertical plane). AIC waves are generated as a result of the strong temperature anisotropy downstream of the shock. The AIC waves there give way to current tubes aligned with the magnetic field (shown on the left of the figure) via the filamentation instability. (From Alexandrova et al., 2004).

However, detailed comparisons of this non-linear instability with theoretical models, including kinetic effects, will form part of future studies.

3.4 Mirror Mode Theory and Modelling

Mirror modes, as described in Section 3.2.1, frequently occur in the magnetosheath under conditions of enhanced ion temperature anisotropy ($T_\perp > T_{||}$) and high $\beta_{\perp i} \sim 2$. They are non-propagating magnetic bottle structures, characterised by large amplitude variations in the magnetic field magnitude, $\Delta B/B \sim 1$, anti-correlated with variations in the plasma number density introducing inhomogeneity into the plasma. Anticorrelation between magnetic field and density perturbations is not unique to mirror modes. It is also typical of slow mode waves, and can lead to large amplitude soliton chains (as has recently been shown by Stasiewicz, 2004), in which case no anisotropy is required. Such structures may appear in the solar wind. In the magnetosheath, mirror modes are dominant because the presence of the large anisotropy and high plasma temperature, damps slow mode waves. It has been suggested that such large amplitude variations might be a significant source of turbulent energy (Pokhotelov et al., 2003).

Previous studies of mirror modes have been limited to the use of single and dual spacecraft. However, four spacecraft Cluster data, available for a variety of tetrahedron scales, allow analysis of mirror structure three-dimensional shape and size that have not previously been possible.

3.4.1 Brief review of mirror mode theory

The existence of mirror modes was predicted by Rudakov and Sagdeev (1959) and Chandrasekhar et al. (1958) from anisotropic plasma fluid theory followed by kinetic approaches by Tajiri (1967), Hasegawa (1969), and Pokhotelov and Pilipenko (1976).

The starting point in a quasi-hydrodynamic approach is the pressure equilibrium condition for an anisotropic plasma

$$\delta p_\perp + \frac{B\,\delta B_\parallel}{\mu_0} = -\frac{k_\parallel^2}{k_\perp^2}\left[1+\frac{1}{2}(\beta_\perp - \beta_\parallel)\right]\frac{B\,\delta B_\parallel}{\mu_0}. \tag{3.4}$$

Here $\delta p_\perp$ is the variation of the perpendicular plasma pressure, $B = |\boldsymbol{B}|$ is the magnitude of the ambient magnetic field $\boldsymbol{B}$, $\delta B_\parallel$ is the compressional magnetic field perturbation, $k_\perp$ and $k_\parallel$ are the components of the wave vector $\boldsymbol{k} = (k_\perp, k_\parallel)$ perpendicular and parallel to the ambient field, respectively, and μ_0 is the free space permeability. The ratio of kinetic to magnetic energy density is given by $\beta = nk_BT/(B^2/2\mu_0)$, with indices $\perp, \parallel$ indicating perpendicular or parallel pressures; n is the plasma number density. The perturbed quantities in Equation (3.4) are assumed to vary in both time and space as $\sim \exp(-i\omega t + i\boldsymbol{k}\cdot\boldsymbol{r})$, where $\omega \ll \omega_{ci}$ is the wave frequency.

The variation in the perpendicular plasma pressure is obtained from the perturbed particle distribution (Pokhotelov et al., 2001)

$$\delta F_j = -\frac{\mu\,\delta B_\parallel}{B}\frac{\partial F_j}{\partial \mu} + q_j\phi\frac{\partial F_j}{\partial W} - \frac{\omega(q_j\phi + \mu\,\delta B_\parallel)}{\omega - k_\parallel v_\parallel}\frac{\partial F_j}{\partial W} \tag{3.5}$$

where $F_j(W,\mu)$ is the particle distribution function which depends on the energy, W, and magnetic moment, μ, of the jth species of mass m_j, charge q_j and parallel speed $v_\parallel = \sigma[2(W-\mu B)/m_j]^{\frac{1}{2}}$ ($\sigma \pm 1$ and indicates the direction of $v_\parallel$). Here, ϕ is the scalar potential, with the wave electric field given by $E_\parallel = -ik_\parallel\phi + i\omega A_\parallel$, $A_\parallel$ being the parallel vector potential.

The ordinary ion-mirror mode is only one of the possibly unstable solutions of the dispersion relation (Pokhotelov et al., 2003) resulting from pressure balance and Maxwell's equations $\mathsf{D}(\omega,\mathbf{k})\cdot\Psi = 0$ for the wave field vector Ψ, whose components are

$$\Psi_\parallel = A_\parallel - \frac{k}{\omega}\phi, \quad \Psi_A = -\frac{k_\perp}{\omega}\phi, \quad \Psi_M = \frac{(\mathbf{k}\times\mathbf{A})_\parallel}{k_\perp} - \frac{k_y\kappa_B}{k_\perp\omega}\phi \tag{3.6}$$

The last term includes the background magnetic field inhomogeneity $\kappa_B = |\nabla \ln B|$ which yields the drift frequency $\omega_D = (k_y v_\perp^2/2\omega_{ci})\kappa_B$. The simplest case, neglecting the drift frequency contributions and assuming a two component Maxwellian plasma with cold electrons, yields the ordinary ion-mirror mode which becomes

unstable when the pressure anisotropy $A \equiv p_\perp / p_\parallel$, satisfies

$$A - 1 > \beta_\perp^{-1} \tag{3.7}$$

$\beta_\perp = 2\mu_0 n k_B T_{i\perp}/B^2$ is the perpendicular ion β, and the electrons do not play any role in the instability. The growth rate of this mode (Hasegawa, 1969) is proportional to the ratio $(k_\parallel/k_\perp)^2$ where $(k_\parallel/k_\perp)^2 \ll 1$. The **k**-vector is thus nearly perpendicular to the magnetic field and the mode has a small growth rate. However, because it is practically non-propagating and is therefore convected with the plasma flow, it has plenty of time to grow and so can reach large amplitudes which ultimately cannot be described by simple linear theory. In the limit of $T_e \to 0$, theory predicts that the cold electrons will wipe out any parallel electric field and therefore that $k_\parallel$ should be zero and the mode cannot exist. However, a small but finite temperature of the electrons will allow for the mode to exist in slightly oblique direction (Pantellini and Schwartz, 1995; Pokhotelov et al., 2001, 2003, 2004).

The ordinary ion-mirror mode grows fastest Pokhotelov et al. (2004) at perpendicular wavelengths comparable to the ion gyroradius, $k_\perp \rho_i \sim 1$. The above threshold for the short wavelength mirror mode is higher by a factor of 2 than in the very long wavelength case $k_\perp \rho_i \ll 1$. Thus, depending on the anisotropy, the fastest growing waves will be those which have a wavelength just long enough for the anisotropy to exceed the instability threshold. The inclination of the mode with respect to the magnetic field implies that the bottles are no longer symmetric around the field direction. Field aligned currents should flow within the structure, generating a non-coplanar magnetic field component, which twists the mirror mode magnetic field around the bottle.

The mirror mode is never observed in the state of linear small magnetic field compressions. Magnetic field compression ratios of 30-80% are observed, deep in the nonlinear regime. Since the mode is non-oscillatory, it is unsurprising that a quasilinear approach (Treumann and Baumjohann, 1997) does not explain the observations. That particle trapping occurs has been suggested by Kivelson and Southwood (1996). Such trapping is inferred from lion roar excitation (Treumann et al., 2000) and observation within mirror modes (Baumjohann et al., 1999), as well as by direct electron observation (Chisham et al., 1998). It has been recognised recently (Treumann et al., 2004) that in the nonlinear marginally stable state the mirror modes should evolve into three-dimensional cylindrical structures with zero parallel wave number extended along the ambient magnetic field. Any remaining inclination with respect to the field then indicates that the mode is still in evolution.

3.4.2 Nonlinear static bottle model of mirror modes

Constantinescu (2002) used the marginal mirror equilibrium condition to consider the stationary equilibrium state of a mirror bottle. Pressure equilibrium in the

plasma reference frame is written

$$\nabla\left(p_{\perp}+\frac{B^2}{2\mu_0}\right)+\nabla\left[\left(p_{\parallel}-p_{\perp}-\frac{B^2}{\mu_0}\right)\frac{\mathsf{B}}{B^2}\right]=0 \tag{3.8}$$

where μ_0 is susceptibility, B magnetic field strength, B is a tensor with elements $(\mathsf{B})_{ij}=B_iB_j$, and $p_{\parallel}$ and $p_{\perp}$ are plasma pressure components. The temperature anisotropy in a bi-Maxwellian plasma is

$$A(\mathbf{r})=\frac{T_{\perp}(\mathbf{r})}{T_{\parallel}(\mathbf{r})}=\left[1-\left(1-\frac{1}{A_0}\right)\frac{B_0}{B(\mathbf{r})}\right]^{-1} \tag{3.9}$$

where $A(\mathbf{r})$ and $B(\mathbf{r})$ are the final anisotropy and magnetic field, and A_0 and B_0 are unperturbed anisotropy and magnetic field. Equation (3.9) holds for 2 (Lee et al., 1987) and 3 (Constantinescu, 2002) dimensions.

In cylindrical symmetry: $\rho,z,\partial/\partial\varphi=0$, one has $\mathbf{B}(\rho,z)=(B_0+\delta B_z(\rho,z))\,\mathbf{e}_z+\delta B_{\rho}(\rho,z)\mathbf{e}_{\rho}$, leading to a set of Bessel differential equations

$$\rho^2\frac{d^2}{d\rho^2}\delta B_{\rho}^n+\rho\frac{d}{d\rho}\delta B_{\rho}^n+\left[\left(\frac{n\alpha\rho}{L}\right)^2-1\right]\delta B_{\rho}^n=0 \tag{3.10}$$

where α is a dimensionless parameter:

$$\alpha=\pi\sqrt{\frac{\frac{1}{2}\left(1-\frac{1}{A_0}\right)+\frac{1}{\beta_{0\perp}}}{A_0-1-\frac{1}{\beta_{0\perp}}}} \tag{3.11}$$

and $\beta_{0\perp}$ is the plasma parameter, i.e., the ratio between the orthogonal plasma pressure, $p_{0\perp}$ and the magnetic pressure, $B_0^2/2\mu_0$.

The solution of Equation (3.10)

$$\{\delta B_{\rho}^n(\rho),\delta B_z^n(\rho)\}=\{\frac{i\pi}{\alpha}C_nJ_1\left(\frac{n\alpha\rho}{L}\right),C_nJ_0\left(\frac{n\alpha\rho}{L}\right)\} \tag{3.12}$$

holds for $\alpha^2>0$, and for physically realistic solutions $C_{-n}=C_n^*$. In terms of the initial anisotropy and plasma β this is equivalent to:

$$A_0>1+\frac{1}{\beta_{0\perp}}\qquad\text{or}\qquad A_0<\frac{\beta_{0\perp}}{\beta_{0\perp}+2} \tag{3.13}$$

The first inequality in Equation (3.13) is the mirror instability condition, and the second the firehose condition (cf, e.g., Baumjohann and Treumann, 1996).

Figure 3.12 shows the onion layer like structure of the magnetic field of a mirror mode bubble. For values of ρ for which $J_1(\rho)=0$, the field lines become straight

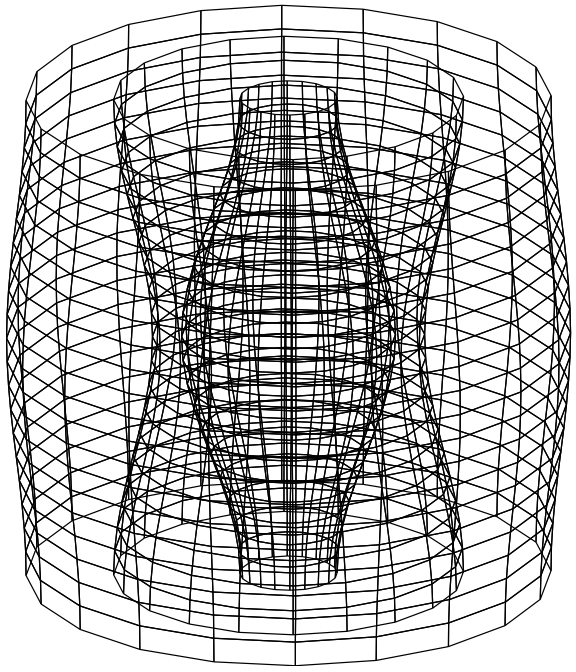

Figure 3.12. Magnetic field surfaces of the first Fourier component of the magnetic mirror perturbation. The main structure, closest to the axis, has a typical bottle shape. Moving radially away from the axis one encounters a series of nested structures which have a similar symmetry to the central one. The surfaces shown in the figure represent surfaces of constant magnetic field, with the field increasing radially outward from the axis. The ambient field direction in this model is parallel to the axis. (From Constantinescu, 2002).

lines on the surface of the cylinder, defining the border between two layers of opposite curvature. The position of the first border, which defines the main structure, is given by the ratio of radius to length of the central bubble

$$\alpha R/L = 3.832 \tag{3.14}$$

and α thus determines the elongation of the bubble.

3.4.3 Fitting model to data

Fitting the model to measured mirror magnetic field allows for the determination of the dimensions of a mirror bubble in equilibrium and the determination of the bubble structure (Equation 3.14). For two reasons the measured mirror field signature is unlikely to contain a significant contribution from more distant layers. Firstly, the amplitude of the Bessel functions decays rapidly with increasing radial distance; and secondly the magnetic field at larger distances from the core of the structure is likely to be affected by the interaction of neighbouring mirror modes. Application

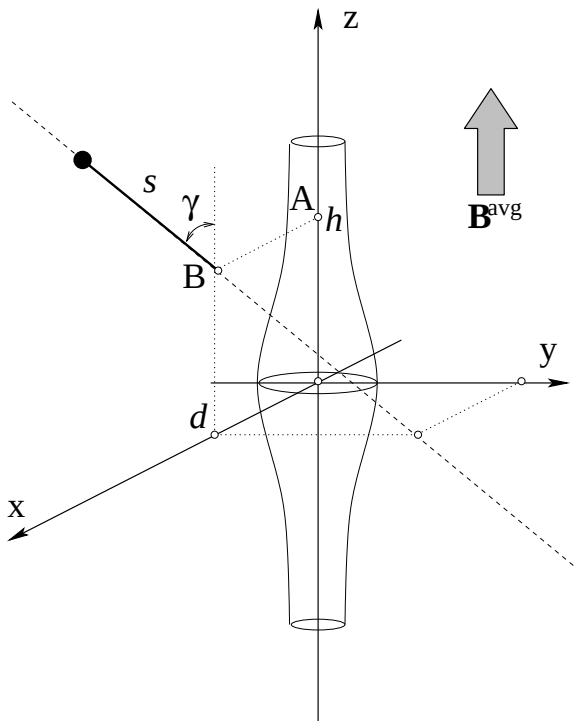

Figure 3.13. The normal coordinate system. The dashed line is the spacecraft path which intersects the (x-z)-plane of the MMS system in the point B(d,0,h) and is parallel with the (y,z)-plane. The angle between the trajectory and the z-axis is γ and the distance between the spacecraft and the point B is s. (From Constantinescu et al., 2003).

of the method requires the introduction of a normal coordinate system (h,d,γ,s) (see Figure 3.13) in which the spacecraft track is parallel to the (y,z)-plane. In these coordinates the spacecraft trajectory can be defined by three parameters: the angle $\gamma \in [0,\pi/2]$ between spacecraft path and the axis of the mirror mode structure (MMS); the distance $d \in [0,\infty)$ between spacecraft path and the MMS axis; and the distance $h \in [-L,L]$ between the centre of the MMS and point A in Figure 3.13. The position of the spacecraft relative to the MMS is then specified by one additional coordinate: $s \in (-\infty,+\infty)$, which is the distance between the point B in Figure 3.13 and the spacecraft.

The parameters used for the fitting are: trajectory normal coordinates (h,d,γ), initial spacecraft position on its path (s_0), length of the MMS (L), the unperturbed magnetic field intensity (B_0) and α. Components up to $n \leq 4$ in the Fourier expansion of the fields have been included. Higher orders merely reproduced irrelevant 'small scale' fluctuations.

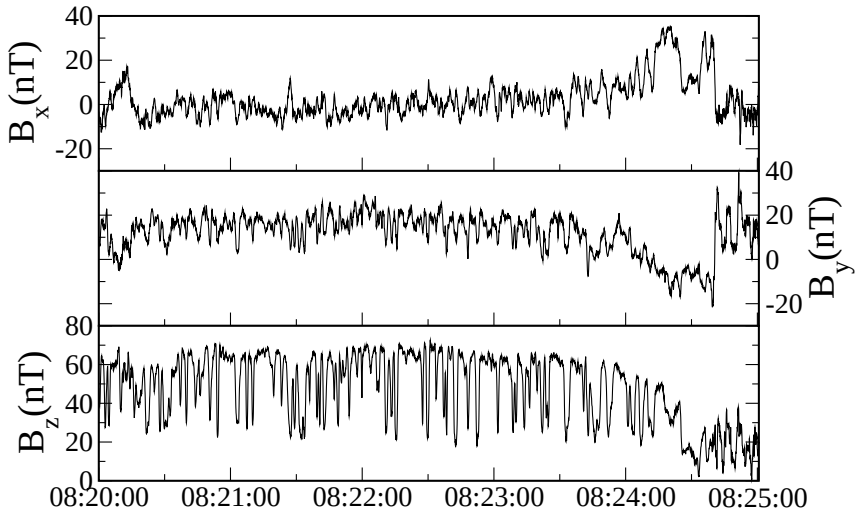

Figure 3.14. Magnetic field data in GSE coordinates from C1 on November 10, 2000 between 08:20 and 08:25 UT. Panels show the magnetic field components at 22 vectors/sec. (Figure provided by D. Constantinescu).

The fit to the data from a single spacecraft is sensitive to the initial choice for the parameters yielding a non-unique solution. With the availability of Cluster data, this ambiguity was avoided (Constantinescu et al., 2003) by simultaneously fitting data from $1 < n \leq 4$ spacecraft. After having identified an MMS from one 'reference spacecraft', and knowing the normal coordinates of the others the model magnetic field for the remaining $4-n$ 'witness' spacecraft can be determined and the correlations constructed between the measured magnetic field and the model magnetic field.

3.4.4 Case study

In the way described above, Constantinescu et al. (2003) analysed an interval of strong mirror wave activity (Lucek et al., 2001) from November 10, 2000 08:20-08:25 UT (Figure 3.14). Cluster was in the dusk side magnetosheath with a typical spacecraft separation of 1000 km, moving at GSE velocities about 1 km s^{-1}. Using correlation analysis, corroborated by Wind observations, Lucek et al. (2001) concluded that the plasma flow velocity was of 815 km s^{-1} in the direction C1 - C3.

Magnetic field data at a resolution of 22 vectors per second were analysed using a fitting window with a width of 200 data points, corresponding to about 9 s or 7000 km. Depending on the values of L and α (Equation 3.14) this corresponded to several layers of the MMS. Assuming that $L = 5000$ km the spacecraft would

have passed through 1-2 layers for $\alpha = 5$, and through 3-4 layers for $\alpha = 10$. In order to identify subintervals where the fit procedure was stable with respect to small changes in the data selected for analysis a sliding window technique was applied and the variability in the resulting parameters examined.

The fit produced a set of parameters for the data subinterval $[i, i+200]$. Those cases where the minimisation converged and the parameters had physically reasonable values were used as start parameters for the next data subinterval $[i+n, i+n+200]$. Otherwise the default values were used. A value of $n = 2$ (99% overlapping intervals) was normally used.

The subinterval 08:20:00 - 08:20:10 UT is shown in detail. Here agreement between the model and the witness spacecraft was reasonably good. The reference spacecraft C1 and spacecraft C2 were chosen to participate in the fit. C3 and C4 were chosen as witness spacecraft. C1 and C2 had a large separation in the direction orthogonal to the average magnetic field, and were expected to sample different MMS layers. The velocity vector was aligned with the C1 - C3 separation vector, as shown in the investigation of mirror modes by Lucek et al. (2001), and so the magnetic field measured by C3 was very similar to the magnetic field measured by C1. As a consequence the magnetic field measured by C3 did not contribute any additional information to the fit. A comparison between the measured and model magnetic field intensity for each spacecraft produced the following cross correlation coefficients: $C_1 = 0.81$, $C_2 = 0.83$, $C_3 = 0.78$, $C_4 = 0.64$. The radius of the main structure was found to be $R = 2061$ km. It is interesting to note that this is larger than what had previously been determined from Cluster observations of mirror modes in the magnetosheath. Lucek et al. (2001) in their investigation of the same day found from correlation analysis that, although variable, the observed mirror structures showed differences on scales of 750-1000 km at spacecraft separated along the magnetic field, while the mirror mode radii appeared to be less than 600 km. Their extent along the flow, however, was of the order of 1500-3000 km. Possibly the correlational method favours the smaller scale local structures while the model assumption provides larger and more global properties.

Figure 3.15 shows the measured and model magnetic field intensities. The vertical continuous lines mark the intersection with the XZ plane, i.e., the time when the distance (d) between spacecraft and the axis of the MMS was minimum. The vertical dotted lines mark the boundaries between different layers. Multiple minima result from passing through different regions of the same magnetic mirror structure. This can also be seen from Figure 3.16, which shows the way in which the spacecraft passes through the layers of the structure.

Figure 3.17 shows the reconstructed magnetic field in the XZ plane. This figure reveals that C1, C3 and C4 probably passed through a central uniform field region of the structure yielding plateaus in Figure 3.15. C2 was much closer to the axis measuring large changes in the magnetic field inside the central structure.

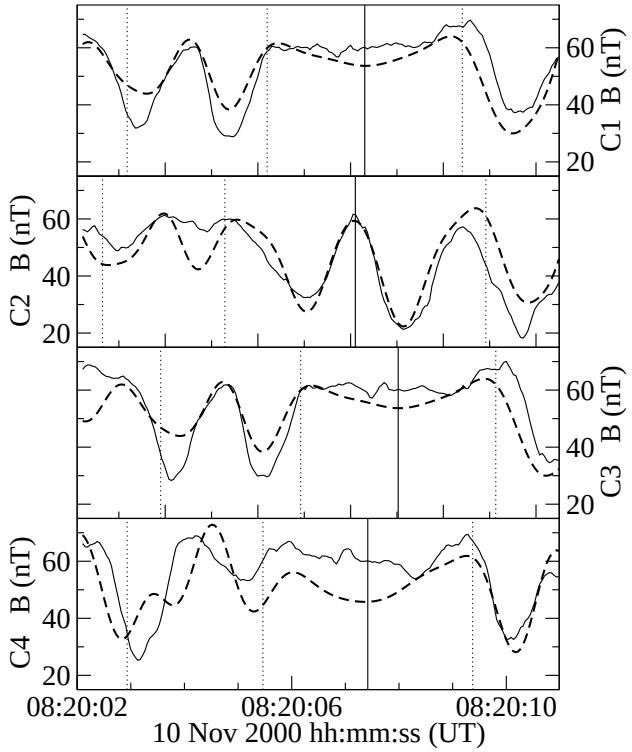

Figure 3.15. Measured (solid lines) and model (dashed lines) magnetic field intensity for the four Cluster spacecraft. C1 and C2 were participating in the fit, C3 and C4 were witness spacecraft. The vertical solid lines represent the intersection with XZ plane (i.e., $s = 0$) and the vertical dotted lines separates different layers of the MMS. (From Constantinescu et al., 2003).

The quality of the parameters can be improved by performing new fits, using data from all four spacecraft and the previous parameters as start parameters. For this particular event, however, Constantinescu et al. (2003) found that no improvement could be achieved. Of course, these values should taken with caution. The precision of the fit to the measurements though being robust contains a number of systematic errors. First, there are the assumptions of the model: it is two-dimensional, assumes stationarity and stability in a non-linear sense, and does not include Finite-Larmour-Radius effects or any kinetic effects. Each of these assumptions has to be proved. Moreover, the model is applied here to only one single mirror structure. The agreement is reasonable, though the Figures 3.15 and 3.16 show that there remain large uncertainties in the fit and the form of the structure relative to the paths of the spacecraft. Hence a conservative conclusion is that the model is still too rough to unambiguously reproduce mirror structures. In future it will be improved in different directions, in particular by applying it to a larger statistical ensemble.

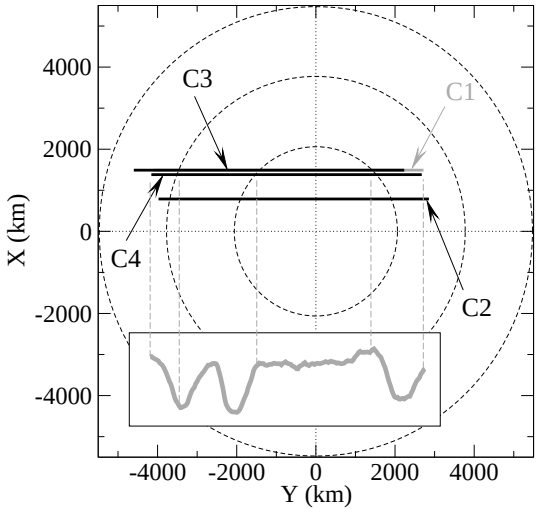

Figure 3.16. The projections of the spacecraft trajectories in the (x-y) plane(straight lines) and the magnetic field measured by C1 (gray curve). The circles represent the boundaries between different layers of a mirror mode structure. (From Constantinescu et al., 2003).

Horbury et al. (2004) recently performed a statistical survey of anti-correlated magnetic field and density structures observed in the magnetosheath. Their study estimated the motion of 39 isolate magnetic dips and 12 peaks, spread over four days, using the application of four-spacecraft timing analysis. Their results were not therefore dependent on the use of a particular mirror mode model. The important finding is that within timing errors the most probable (average) velocity is very close to zero indicating that the structures are convected with the flow. The scattering of the velocity was $\sim 21\,\mathrm{km\,s^{-1}}$ much less than the local wave speeds ($<$5% of the local Alfvén speed and $<$15% of the local slow mode velocity). Hence, observations do not support the view that propagating slow mode waves or solitons are responsible for the formation of such structures in the magnetosheath. Neither are they standing structures, i.e., propagating against the flow. The directions of the normals derived for the mirror modes from timing analysis were consistent with the structures having a cylindrical cross section, inclined by a small angle ($< 20^{\circ}$) to the background magnetic field. These results, therefore, suggest a mirror mode geometry more similar to the idealised model presented in this section, rather than a soliton model, where the structures would be expected to be sheet-like.

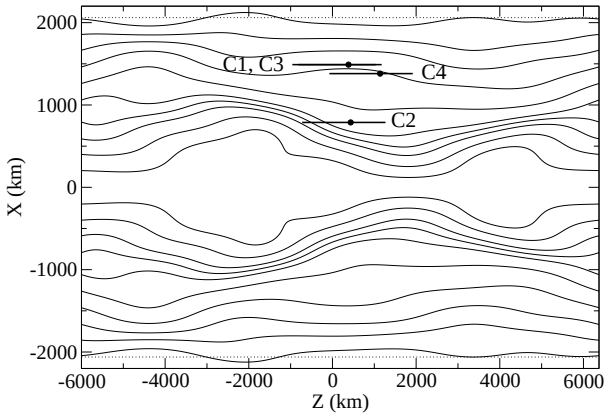

Figure 3.17. The magnetic field lines derived from the model of a mirror mode structure. The straight lines are the projections of the spacecraft trajectories on the XZ plane. The dots are the points where the spacecraft paths intersect the XZ plane. (From Constantinescu et al., 2003).

3.5 Observations of High-Frequency Waves

3.5.1 Electromagnetic waves: Lion roars

Lion roars are intense, short-duration, narrow-band packets of whistler mode waves observed in Earth's magnetosheath, first reported by Smith et al. (1967) using data from OGO 1. The average mean frequency of these waves in the magnetosheath is ~ 100 Hz (0.25-0.5 f_{ce}) with typical amplitudes of 0.1 nT and burst durations of 1 - 2 s (Smith and Tsurutani, 1976). When Lion roars are excited inside mirror modes, their frequency is much lower because of the strongly depressed magnetic field. A more detailed study of lion roars found that these emissions were most often observed in the inner region of the sunward magnetosheath, and the distribution of their intensity at 200 Hz was highest near the subsolar magnetopause (Rodriguez, 1985). Tsurutani et al. (1982) found that lion roars often coincide with minima of the magnetic field strength and maxima of plasma density, indicative of mirror mode structures. Zhang et al. (1998), using large amounts of data collected by the Geotail spacecraft, argued that only 30% of the lion roars were associated with mirror modes. This was probably due to a selection effect of the magnetometer aboard Geotail as discussed by Baumjohann et al. (1999) who, using the very sensitive magnetometer on Equator-S, found that low frequency lion roars are nicely associated with mirror modes. They consist of very narrow band emissions of a few tens of Hz frequency following the local electron cyclotron frequency and indicating the presence of trapped electrons in mirror modes. Lion roars are most probably gener-

ated by unstable anisotropic electron distributions, when the perpendicular electron temperature is larger than the parallel temperature. These are the low parallel energy electrons. In the mirror mode structures, the number of resonant electrons is larger for a given anisotropy than outside in the undisturbed magnetosheath (Smith and Tsurutani, 1976).

Early studies of lion roars in the magnetosheath found that they typically propagate with wave vectors at angles less than 30° relative to the magnetic field (Smith and Tsurutani, 1976). Baumjohann et al. (1999) found that the wave vectors were very close to parallel to the magnetic field, taking into account measurements of nearly monochromatic magnetic wave packets detected by the Equator-S spacecraft in the minima of the magnetic field. Some of the lion roars contained in the Geotail study (Zhang et al., 1998) were found to have wave vectors near 90°, suggesting they were downstream propagating whistler waves from the bow shock. Zhang et al. (1998) also found that although the majority of lion roars that were detected by Geotail were propagating in one single direction, one class of lion roars were found to be propagating in two directions simultaneously, suggesting the local plasma as the source.

The multipoint measurements of Cluster are ideally suited for determining the location of the source region and characteristics of the magnetosheath lion roars. Maksimovic et al. (2001), using data obtained in the duskside magnetosheath from the Cluster STAFF Spectrum Analyser (Cornilleau-Wehrlin et al., 1997), found that close to the magnetopause, lion roars in deep magnetic troughs are observed to propagate simultaneously in two directions, both parallel and anti-parallel to the magnetic field, as shown in Figure 3.18. Panels (a) and (b) of this figure show that the lion roars (solid line) are found to be more circular and more right-handed than the other whistler waves (dotted line). Panel (c) shows two peaks for the wave vector of the lion roars. After taking into account Doppler effects and the plasma velocity, these results imply that some lion roars on this date were propagating both upstream and downstream. This suggests that the Cluster spacecraft were in the source region of the lion roars, consistent with the results of Zhang et al. (1998). Far from the magnetopause, the waves were found to propagate in only one direction, roughly anti-parallel to the magnetic field. In addition Maksimovic et al. (2001) found that the lion roars were propagating at angles of 30° to 50° from the local magnetic field direction, which is inconsistent with whistler mode waves which would normally be Landau damped in a bi-Maxwellian plasma. This differs from many of the earlier works which found much smaller angles, and may be due to the sampling and bandwidth characteristics of the STAFF-SA instrument. It is also possible that this angular difference has a physical explanation that will become apparent through future statistical studies of lion roars. One should, however, take into account that the time resolution of the Cluster measurements is conciderably lower than that of the Equator-S measurements, and because of this, the direction finding is less accurate for Cluster measurements than for Equator-

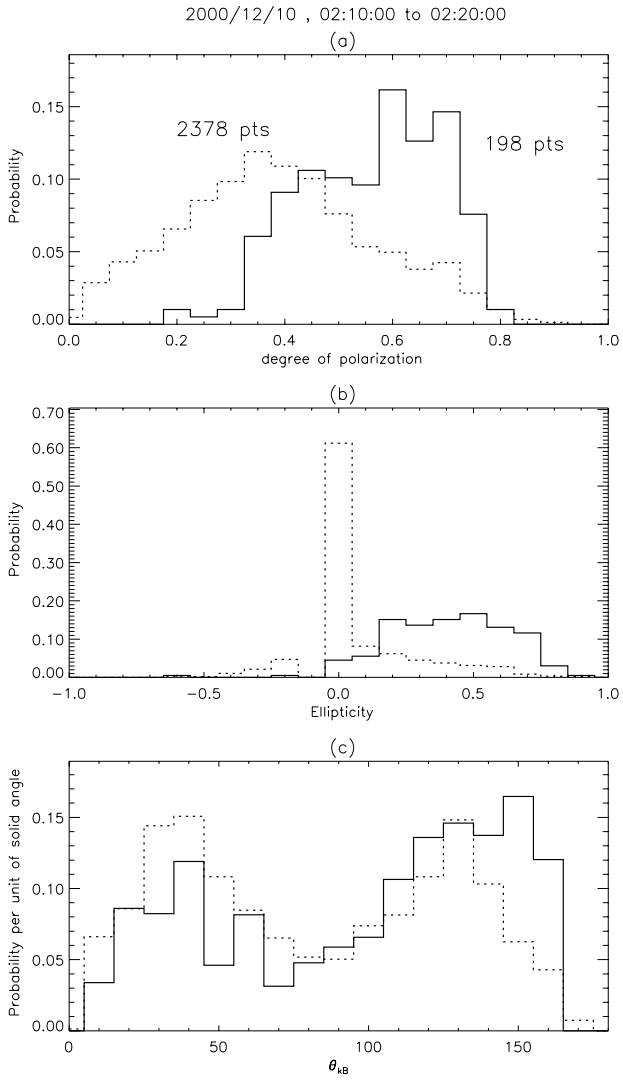

Figure 3.18. Histograms showing various characteristics of the whistler waves observed on December 10, 2000 near the magnetopause by the STAFF-SA instrument on the Cluster spacecraft: (a) the degree P of polarisation, with a value of 1 indicating the three components are fully coherent and the wave field is fully polarised, (b) the ellipticity (+1 for circular right-hand polarisation), and (c) the angle between the wave vector and B_0, for the lion roars (solid line) and for other whistlers (dotted line). (From Maksimovic et al., 2001).

S, as discussed by Baumjohann et al. (1999) with respect to the measurements of Zhang et al. (1998) for lion roars related to mirror modes. The more sensitive magnetometer aboard Equator-S which allowed for extraordinarily high time resolution clearly identified narrow band low frequency lion roars to propagate very close to parallel or antiparallel to the local magnetic field thus suggesting that the lion roars observed in relation to mirror modes originate from various trapped electron components in different places inside mirror mode bubbles.

The work of Maksimovic et al. (2001) was an introductory study of lion roars using the Cluster fleet. The primary contribution that Cluster can make to the knowledge already gained on the characteristics of lion roars is performing a statistical study of the direction of propagation using the multi-spacecraft measurements of STAFF-SA obtained in various regions of the magnetosheath as well as outside and inside mirror modes. These measurements will be supplemented with information obtained from various Cluster instruments, such as FGM, to determine the fraction of lion roars observed within mirror mode structures, or PEACE to determine whether an electron temperature anisotropy exists for those lion roars observed to be propagating in two directions. In addition, the very high time resolution waveform data of the Wideband (WBD) plasma wave receiver (Gurnett et al., 1997) should help in this regard. Since WBD has a time resolution of 35 μs and time of measurement accuracies to 10 μs on all 4 spacecraft, cross-spacecraft correlations of the lion roar waveforms can be performed, yielding information on the propagation of these lion roar wave packets from the source region. A similar correlation analysis has been successfully carried out for the chorus emission region in the inner magnetosphere (Santolik and Gurnett, 2003).

3.5.2 Electrostatic waves: Broadband structures

All of the early plasma wave measurements made by spectrum analyzers showed the prevalence of Broadband Electrostatic Noise (BEN) in many regions of Earth. First discovered by Scarf et al. (1974) and Gurnett et al. (1976) in the distant tail of Earth, BEN was characterized as being bursty and consisting of broadband spectral features usually extending from the lowest frequencies measured up to as high as the plasma frequency. The intensity of BEN was found to decrease with increasing frequency. Rodriguez (1979) provided the first comprehensive survey of BEN in the magnetosheath. He found that the magnetosheath electrostatic turbulence was almost continually present throughout the magnetosheath with broadband (20 Hz to 70 kHz) rms field intensities typically 0.01 - 1.0 mV m^{-1}. He also found the turbulence to consist of two or three components: a high frequency component ($\geq$ 30 kHz) peaking at the electron plasma frequency f_{pe}, a low frequency component with a broad intensity maximum below the nominal ion plasma frequency f_{pi}, and a less well defined intermediate component in the range $f_{pi} < f < f_{pe}$.

Dubouloz et al. (1993) carried out a theoretical investigation that showed that electron acoustic solitons passing by a satellite would generate spectra that could explain the high frequency part of BEN, above the electron plasma frequency, that had been observed in the dayside auroral zone by the Viking satellite. This was followed in 1994 by the findings of Matsumoto et al. (1994) that solitary waves of a few milliseconds in duration were responsible for the high frequency part of BEN observed by the Geotail satellite in the plasma sheet boundary layer. These electrostatic solitary waves appeared in the form of bipolar pulses (one positive electric field peak followed by one negative peak, or vice versa) in the time series data obtained by the Geotail Plasma Wave Instrument. An electron two-stream instability that produced nonlinear Bernstein-Greene-Kruskal (BGK) type isolated potentials was proposed by Matsumoto et al. (1994) as the generation mechanism for the electrostatic solitary waves. The Fourier spectrum of the solitary waves represented by the bipolar pulses was thus the reason for the broad band signature since a single pulse contains all frequencies up to a frequency determined by the time duration of the pulse. Subsequently similar solitary waves were found to be responsible for the BEN observed in several other regions of Earth, c.f. Franz et al. (1998) and Ergun et al. (1998) using Polar and FAST satellite data, respectively. Interferometry data obtained on these satellites allowed for the identification of these solitary waves as coherent potential structures, either electron or ion phase-space holes determined by the direction of propagation of the solitary waves, the hemisphere in which they were detected, and the initial direction (positive or negative electric field) of the pulses. A statistical survey of electron solitary waves observed by the Polar satellite at 2 to 9 R_E was carried out by Cattell et al. (2003) with the following findings: 1) the mean solitary wave duration was about 2 ms; 2) the waves have velocities from $\sim 1000\,\mathrm{km\,s^{-1}}$ to $> 2500\,\mathrm{km\,s^{-1}}$; 3) the observed scale sizes (parallel to the magnetic field) are on the order of 1-10 λ_D, with $e\phi/kT_e$ from ~ 0.01 to $O(1)$.

Cluster observations of solitary waves in the magnetosheath were first reported by Pickett et al. (2003). Using Cluster WBD data (Gurnett et al., 1997), the bipolar pulse solitary waves were found to have time durations of $\sim$25-100 μs in the dayside magnetosheath near the bow shock. These solitary waves were found to be consistent with electron phase space holes. They were detected when the magnetic field was contained primarily in the spin plane, indicating that they propagate along the magnetic field. It was not possible for Pickett et al. (2003) to determine the velocity of the structures since the Cluster WBD instrument makes a one axis measurement, that being the average potential between the two electric field spheres. It was also not possible to correlate individual solitary pulses across different Cluster satellites, due to the 1/8 duty cycle of the WBD instrument when using this wideband 77 kHz filter mode and/or the solitary waves evolving (growing/damping) over the distance from one spacecraft to the next. Limited success of correlating solitary waves across satellites has been attained thus far only for the tripolar type

solitary wave (discussed below) observed in the auroral region at 4.5 - 6.5 R_E, well above the auroral acceleration region (Pickett et al., 2004b).

By using spectrograms of the waveform data obtained from two of the Cluster spacecraft separated by over 750 km in the magnetosheath, Pickett et al. (2003) found that the overall profile of the broad-band noise associated with the solitary waves was remarkably similar in terms of onset, frequency extent, intensity and termination on both spacecraft. This similarity implies that the generation region of the solitary waves observed in the magnetosheath near the bow shock is very large. The generation region may be located at or near the bow shock, or it may be local in the magnetosheath but related to processes occurring at the bow shock. Figure 3.19 shows an example of the broadband structures observed during a Cluster magnetosheath pass at high magnetic latitude on 05 April 2004 when the spacecraft were separated by as little as 150 km (spacecraft 1 and 2) and by as much as 500 km (spacecraft 1 and 4). The top three panels contain data from each of Cluster spacecraft 1, 2 and 4 showing the broadband structures spanning the range from the lowest frequency measured, 1 kHz, up to as great as 60 kHz. Intense waves around 2 - 3 kHz are also observed throughout the interval. Interference from the emission of electron beams from the EDI experiment shows up as horizontal lines in the Cluster 1 data. The waveforms used to create the spectrograms for each of the spacecraft for a small time period around 13:37:00.33 UT are shown in the bottom three panels. Each panel contains 4 ms of data and except for parts of the bottom two panels, the data shown are from slightly different time periods based on the offset time below each panel from the start time shown at the top of the three panels. Solitary waves of a few tenths of mV m^{-1} peak-to-peak and time durations of around 90 μs are seen to dominate the waveform data leading to the broad bands seen in the spectrograms. Evidence of the 2 - 3 kHz sinusoidal type wave is also seen in the Cluster 1 data. Just as for the case with larger separations reported in Pickett et al. (2003), the overall profiles of the broad-band structures associated with the solitary waves are very similar on all spacecraft. Even so, the solitary waves as seen in the bottom two panels of the figure during the parts that overlap in time do not show a correlation.

Because the Cluster WBD plasma wave receiver is particularly suited to making measurements of solitary waves over a large range of time scales (a few tens of microseconds to several milliseconds) and over a wide range of amplitudes due to its automatic gain control feature, data from this instrument were used (Pickett et al., 2004a) in carrying out a survey of solitary waves observed throughout the Cluster orbit, including the magnetosheath. These solitary waves have been referred to as isolated electrostatic structures (IES) because they are isolated pulses in the electric field waveform data and previous studies have found them to be potential structures propagating primarily along magnetic field lines. Pickett et al. (2004a) found that throughout the Cluster orbit, two dominant types of IES are observed, the bipolar pulse type already discussed, and the tripolar pulse, consisting of one positive and

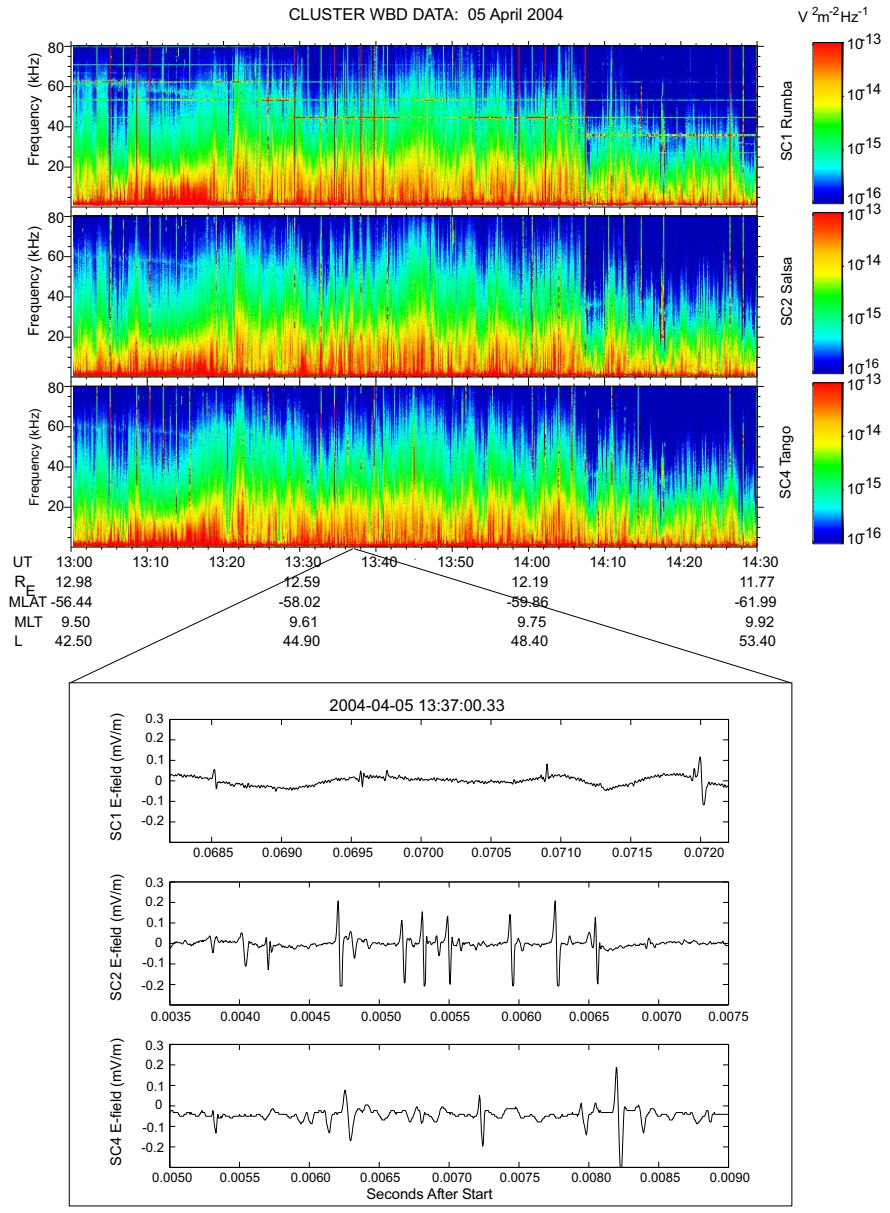

Figure 3.19. Cluster WBD observations of the waves in the magnetosheath. The top three panels contain the data in spectral form produced from high time resolution waveforms obtained on Cluster 1, 2 and 4, respectively, and the bottom three panels show very short time period snapshots of the waveforms from each of these three spacecraft. (From Pickett et al., 2003).

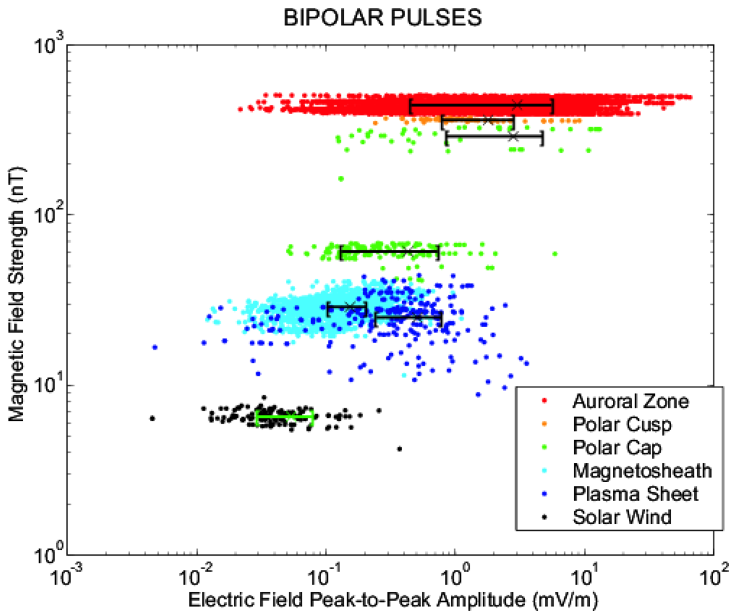

Figure 3.20. Survey of the bipolar pulses observed by Cluster WBD over a two-year period. This plot shows the electric field amplitude vs. magnetic field strength, with the over plotted bracketed lines with the embedded 'x' within each regional grouping representing the standard deviation and mean of that group, respectively. (From Pickett et al., 2004a).

two negative peaks, or vice versa, thought to be weak double layers (Mangeney et al., 1999; Pickett et al., 2004b). In carrying out the survey, Pickett et al. (2004a) found that there is a broad range of electric field amplitudes at any specific magnetic field strength as shown in Figure 3.20 for the bipolar pulses. More surprising was their finding that there is a general trend for the electric field amplitudes of the structures to increase as the strength of the magnetic field in which the measurements are made increases, as shown in Figure 3.20 for the bipolar pulses. A similar trend exists for the tripolar pulses (see Figure 4a of Pickett et al., 2004a). The magnetosheath IES were thus found to have some of the smallest amplitudes observed throughout Cluster's orbit with a mean value of about 0.2 mV m^{-1} since the local magnetic field strength is relatively small there (few tens of nT). Only the IES observed in the solar wind had smaller amplitudes.

An explanation for the relationship between the solitary wave electric field amplitude and magnetic field strength is not yet fully developed. However, Pickett et al. (2004a) considered the possibility that the solitary waves are BGK mode (Bernstein et al., 1957). This being the case, the observed data trend of increasing electric field amplitudes with increasing magnetic field strength could be rooted in the stability requirements of the BGK mode in finite magnetic fields. Chen et al.

(2004) have found a set of inequalities that describe the stability of BGK mode solitary waves. These conditions point to a trend that in a much weaker magnetic field, either the potential amplitude would decrease or the size would increase in order for the structures to be stable, which results in smaller electric field amplitudes.

One other important finding came out of the survey by Pickett et al. (2004a). They found that when the time durations of the bipolar and tripolar IES were plotted with respect to the magnetic field strength, there was no similar trend as with the electric field amplitudes (see Figures 3b and 4b of Pickett et al., 2004a). However, plotting the data in this fashion clearly pointed out that the magnetosheath IES, both bipolar and tripolar, are clearly of much shorter time duration than the structures observed in all the other regions sampled by Cluster, including those in the solar wind. Although Pickett et al. (2004a) speculated that this may imply that the magnetosheath solitary waves are being generated by a different mechanism (perhaps through turbulence rather than a beam instability) than the IES observed in all other regions by Cluster, clearly more work, both experimental and modelling, is required in order to solve this mystery. In particular, the Cluster electron and ion data, together with other wave data, will be evaluated with respect to the observance of solitary waves. These data will then be used as inputs to models seeking to determine the generation mechanism of the solitary waves observed in the magnetosheath. Modelling has been very effective in shedding light on the generation of the solitary waves observed in the auroral acceleration region (for a short review, see Pickett et al., 2003).

3.6 Observations of Dispersed Ion Signatures

Observations made using data from previous missions have shown that Hot Flow Anomalies (HFAs), discussed in some detail in Eastwood et al. (2005), can generate a signature in the magnetosheath (Paschmann et al., 1988; Schwartz et al., 1988; Safránková et al., 2000), and it was found later that they can even affect the magnetopause sufficiently for a ground response to occur (Sibeck et al., 1998, 1999). Recently, however, it has been proposed that in addition to HFAs generating hot, turbulent plasma in the magnetosheath, a different, subtle, interaction between ions reflected from the bow shock and an interplanetary discontinuity can generate dispersed bursts of anomalously high energy particles in the magnetosheath (Louarn et al., 2003). These have been called ‘magnetosheath dispersed signatures’, or MDSs. Louarn et al. (2003) reported energy-time dispersed ion signatures in the magnetosheath observed when Cluster was located over 12 R_E from Earth. They presented CIS and FGM data from three events, noting that more than 20 events occurred during a 2-month period between February and March 2001.

MDSs are characterised by a dispersed ion signature, with the most energetic ions being observed first, with significant fluxes at energies > 5 keV, followed by a decrease in the ion energy over approximately 1-2 min. CIS observations show ions appearing first in the highest energy range of the instrument (30 keV), but RAPID

data indicate that the maximum MDS ion energy extends well above the energy range measured by CIS, up to energies of 30-60 keV. The ion signature of an MDS is not just restricted in energy. The pitch angle distribution is very anisotropic, with the ions systematically organised in a clear ring, with the central axis of the ring close to the magnetic field direction. The 3-D ion distribution, therefore, forms a hollow cone, which has its axis close to the local magnetic field direction. MDS ion distributions can also be non-gyrotropic. Although the ion energy decreases with time during each MDS, the characteristics of the cone do not appear to change systematically throughout the event. The characteristics of the thermal plasma are not affected by the MDS and the absence of Oxygen ions suggest that the spacecraft are not magnetically connected to the magnetosphere during these events.

MDSs are distinct from the magnetosheath signatures of HFAs. The latter are typically characterised by heated plasma, associated with a region of disturbed magnetic field and significant plasma velocity perturbations. The HFA signatures are centered on a change in magnetic field direction and show depressed magnetic field magnitude, flanked by enhancements in $|\mathbf{B}|$ and N_p. The ion flux associated with HFAs at, for example 20 keV can be up to two orders lower than the flux at that energy within an MDS. MDSs do, however, appear to be associated with HFAs signatures in the magnetosheath, and several were observed to occur just before HFA signatures.

Louarn et al. (2003) proposed that the acceleration process generating MDSs is located at the shock. However, the profile of the time-dispersed ion signature cannot be explained just by invoking a time of flight effect from a remote, stationary, source. A model was proposed by which the MDSs ion spectra profiles could be explained by a combination of effects. The first effect arises from the motion of the injection site of the particles along the bow shock. The injection site is assumed to be the region where a discontinuity interacts with the bow shock, and this moves across the bow shock as the discontinuity is convected anti-sunwards by the solar wind. Once they enter the magnetosheath, the motion of the highest-energy ions is dominated by the time of flight effect, so the highest-energy ions arrive first. At the other end of the energy range, motion of lower energy particles is dominated by anti-sunward convection of the plasma, and these particles show almost no time-of-flight dispersion. The combination of these effects is demonstrated by the use of a 2D model to give rise to a particle dispersion profile consistent with MDSs (Figure 3.21).

The organisation of the particles in a ring distribution places some limits on the acceleration mechanism. In addition, since particles are accelerated to >30 keV, into the RAPID energy range, this implies that the acceleration process must be efficient, and occur in only a few gyro-periods. Shock drift acceleration (e.g., Armstrong et al., 1985), which operates at quasi-perpendicular shocks, accelerates particles in only a few gyro-periods, but the energy gain is limited to only a few times the initial particle energy, which is lower than the energy gains observed in MDSs.

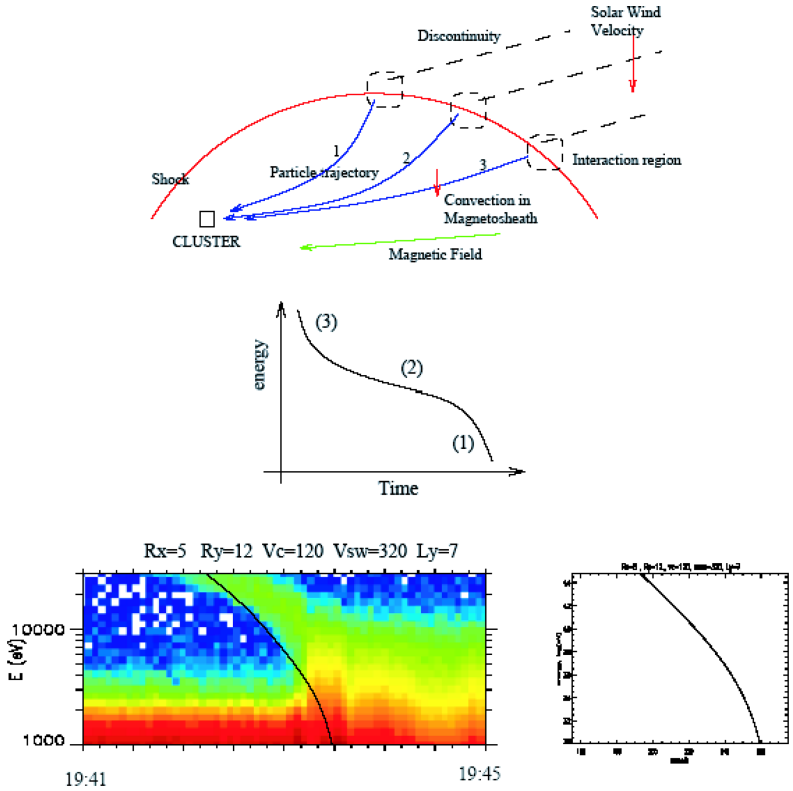

Figure 3.21. A schematic of the interaction between a discontinuity and the bow shock, generating the dispersive ion signature of a magnetosheath dispersed structure. From top to bottom: (1) global configuration of the interaction and example of trajectories (2) typical dispersion calculated from the model and, (3) fit of the observations. (From Louarn et al., 2003).

Fermi-acceleration (Bell, 1978), which operates when particles scatter from irregularities with converging velocities, can lead to greater energy gain, but operates more slowly than shock drift acceleration. In order to explain the observations an acceleration process was proposed which combines aspects of both mechanisms.

The authors estimate that the interaction time between the particles and the shock, during which acceleration occurs, is approximately 100 s. The model is as follows: A fraction of incident solar wind ions are reflected from the shock. Some of these particles are then turned by their interaction with the moving discontinuity, gaining energy in the process, and then re-encounter the shock. A fraction of these particles are also reflected, leading to a further possible interaction with the discontinuity. In this way, multiple bounces between the converging shock face and discontinuity plane lead to energy gains into the 20-30 keV range, as observed at an MDS. A fraction of the particles escapes multiple interactions with the shock,

because they exit the discontinuity at more than 2 Larmor radii from the shock, and hence do not re-cross the shock face.

The proposed process predicts an asymmetry in the source of the particles since the mechanism only operates if the gyratory motion carries the ions further from the shock. Such an asymmetry is observed in MDSs. Also the characteristic pitch angle selection of the energised particles can be explained in terms of the interaction of the particles with the quasi-perpendicular bow shock. Lastly, in this scenario, when the discontinuity interacts with the shock, particles which bounce between the two form the MDS. A further population of particles would form an HFA, and thus give rise to hot turbulent plasma in the magnetosheath which is commonly associated with HFA formation. The two types of magnetosheath signature would reach the observer almost simultaneously, thus explaining why an MDS is often observed as a precursor to the magnetosheath signature of an HFA.

These dispersed structures do not lead to significant pressure disturbances in the magnetosheath, and so they therefore probably play only a minor role in solar wind/magnetosphere coupling. However, a greatly enhanced efficiency of particle acceleration, in time, flux and energy, is achieved through the interaction of ions reflected from a quasi-perpendicular bow shock with the moving interplanetary discontinuity. This demonstrates the potential importance of shock/shock or discontinuity/shock interactions in generating significant fluxes of accelerated particles.

3.7 Summary and Outlook

Cluster has already contributed substantially to our understanding of the physics of the magnetosheath. Though it is not the first time that more than one spacecraft has been used to study the spatial structure of space plasmas, it is the first time that structures in the magnetosheath can be resolved in three dimensions and in the space-time domain, by combining data from the four Cluster spacecraft. In particular the ability to calculate the wave vectors of magnetosheath waves, and to examine the distribution of energy between different modes simultaneously, revolutionises the study of many magnetosheath phenomena, as illustrated by the results presented in this chapter. In addition, more sensitive and sophisticated instrumentation on the Cluster spacecraft, measuring phenomena occurring over a wide range of spatial scales, has opened further new opportunities for research. The richness of the Cluster data set has also allowed new analysis of such fundamental topics as particle acceleration and plasma instabilities. Finally, this chapter demonstrates that Cluster offers us the best opportunity yet to study the highly complex plasma phenomena in this fascinating region.

The main achievements described in this chapter are the following:

1. The unambiguous identification of wave modes present in a broad band magnetosheath fluctuation spectrum. Complementary methods allow the identifi-

cation of the dominant wave mode, together with time variations in the wave mode power. At low frequencies the mirror mode was found to dominate but results at higher frequencies showed that the plasma supported multiple waves simultaneously, and that their wave vectors lay on MHD dispersion curves.

2. The first accurate identification of Alfvén waves generated by proton and alpha particle temperature anisotropies immediately downstream of the quasi-perpendicular shock. In addition, these waves then appeared to evolve into thin current tubes, aligned with the magnetic field. The tubes have a radius of only 100 km - the order of the local ion inertial length, but a length exceeding 600 km. It is proposed that these current tubes are generated from the Alfvén waves, through the action of the filamentation instability.

3. In the highly turbulent magnetosheath plasma the mirror mode is probably the lowest frequency energy source in the turbulence. With Cluster it is possible to make the first estimate of the spatial scale of mirror modes in directions other than along the magnetosheath flow. Results show that they are nearly aligned with the magnetic field and that they have an extent exceeding 1000 km in this direction.

4. Cluster data can also be used to estimate the motion of mirror modes, which are predicted, from theory, to be stationary in the plasma frame. A statistical investigation of a set of mirror structures showed that in general mirror modes are close to stationary in the plasma frame. They are convected by the magnetosheath plasma flow and in this study their remnant plasma frame velocity was found to be much less than the slow mode speed, indicating that they were neither slow modes nor solitons. These observations are also consistent with the mirror modes having a cylindrical cross section. In contrast, analysis of a different time interval as part of a different study, suggests that, under some circumstances, slow magnetosonic solitons can exist in the magnetosheath.

5. Fitting a nonlinear stationary model to an observed mirror structure allows the determination of its scale in different directions. Mirror structure sizes vary between 600-2000 km in diameter and several thousand km in length along the ambient field. Nonlinear theory suggests that they should not be inclined to the magnetic field, and the observation of a small inclination to the magnetic field indicates that they are driven, and are still evolving.

6. In the higher frequency range Cluster observations of lion roars have been analysed, yielding controversial results on their origin. Their propagation seems to be too oblique for whistler mode waves, thereby posing an important problem for future research.

7. Waveforms of broadband electrostatic noise in the magnetosheath between 1 - 60 kHz indicate that most of this noise results from large numbers of phase

space holes; Cluster is the first spacecraft to detect such holes in the magnetosheath. From the similarity of the waveforms and spectra of broadband electrostatic noise on spacecraft separated by several hundred kilometres, close to the bow shock, it is concluded that the noise source region was extended, and that the generation region was probably close to the bow shock.

8. Cluster has detected two types of noise leading to Isolated Electrostatic Structures in the magnetosheath: bipolar and tripolar structures, the latter belonging to weak double layers, showing that the magnetosheath contains small-scale regions of stationary, localised electrostatic fields.

9. Discovery of energy dispersion in ion fluxes originating from the bow shock suggests that in some cases, when an interplanetary discontinuity interacts with the bow shock, energetic ions can bounce between the shock and the discontinuity, and in this way become energised by the Fermi mechanism. A proportion of the hot ions enter the magnetosheath, giving a dispersed burst of energised particles with maximum energies exceeding 30 keV.

Some of these findings are unprecedented and many were possible only with the multi-spacecraft capabilities of Cluster. In the light of these results, in which direction should the Cluster investigation of the magnetosheath go in the near future? It is clear that the multi-spacecraft aspect of Cluster will be essential to future magnetosheath research, even though the instrumentation provides excellent single spacecraft science as well. Many of the studies performed so far will only reach maturity with more extensive analysis of magnetosheath phenomena under the wide range of boundary conditions provided by the solar wind and the magnetosphere. There are many ideas to be pursued:

1. One most tantalizing question is the understanding of the turbulence in the magnetosheath plasma. Cluster provides a unique opportunity to study the spatio-temporal properties of this turbulence, its spatial variation and its wave vector spectrum, at least in the volume of **k**-space made accessible by the range of spacecraft separation scales. The *k*-filtering technique has provided a tool for investigating the dispersion relation of multiple waves present simultaneously in the plasma. Its application demonstrates that multiple wave modes are present in the plasma, and that the relative contributions of the different modes varies with frequency. A complete description of the fluctuation spectrum at all frequencies and all wave vectors is the purpose of active studies. As these are fundamental to all turbulence theory, this is a key topic for study with Cluster. A further opportunity for Cluster is to examine the time evolution of wave modes, for example using the phase difference method which can be applied under circumstances when one wave mode dominates the spectrum.

2. The lowest frequency turbulent mode is the mirror wave. Its complete investigation requires a more precise determination of its scales, growth rates and

saturation mechanisms than available today. This problem can be addressed partially by Cluster. It is of particular interest to decide whether mirror modes are in their final nonlinear state or still evolving; whether they propagate in the low frequency slow mode; what their cause is: either they are unstably excited by the mirror instability, as is believed, or result from an inverse cascade in magnetised plasma turbulence. This requires investigation of the turbulent modes and their interaction, again requiring the spatial properties of the turbulence to be resolved. Particle measurements must also be considered in order to decide what the role the ions and electrons play respectively in the evolution of turbulence in general, and in the development of mirror modes in particular.

3. An interesting question concerning mirror modes is whether, when they are close to the magnetopause, they can trigger reconnection by lowering the magnetic field. However, the observation that mirror modes tend to occur as large amplitude holes near the magnetopause may, on the other hand, suggest that they are themselves the result of the magnetopause reconnection process. Cluster could settle this problem by investigating the properties and propagation characteristics of mirror modes near the magnetopause, and their relation to reconnection.

4. The waves generated by the bow shock form another component of the low frequency magnetosheath fluctuation spectrum. Use of the four spacecraft data together, at a range of separation scales, will allow the waves generated by the bow shock and their subsequent evolution to be analysed in detail, and comprehensive comparisons to be made with predictions from wave and instability theory.

5. An important consideration in the high frequency electro-static range is the nature of phase space holes throughout the magnetosheath. What is their excitation mechanism? Are they related to the bow shock? Are weak double layers formed locally in the magnetosheath? Do they contribute to electron or ion heating? Do they generate transport coefficients which affect the large-scale turbulence or, close to the magnetopause, even reconnection? By combining knowledge of their propagation and orientation with particle observations, Cluster can address some of these questions.

6. Other facets of high frequency electrostartic fluctuations observed by the Cluster wave instrument package in the magnetosheath are yet to be interpreted. For example, intriguing sporadic bursts of a few kHz width, and of short duration (of the order of 100 ms), which are observed at frequencies shifted by a few kHz above the local plasma frequency.

7. The unexpected observation of dispersed ion bursts in the magnetosheath might be one signature of a potentially important mechanism operating at the shock.

They seem to arise from the bouncing of particles between the shock and an oblique discontinuity, as the discontinuity tracks across the shock carried by the solar wind flow. This might be the injection process by which particles are energised, to form a seed population for further Fermi acceleration, a process for which scientists have been searching for many years.

Acknowledgements

Cluster research in the UK and France is supported by PPARC and CNES, respectively. MLG and JP acknowledge support from NASA.

References

Alexandrova, O., A. Mangeney, M. Maksimovic, C. Lacombe, N. Cornilleau-Wehrlin, E. A. Lucek, P. M. E. Décréau, J. M. Bosqued, P. Travnicek, and A. N. Fazakerley: 2004, 'Cluster observations of finite amplitude Alfvén waves and small-scale magnetic filaments downstream of a quasi-perpendicular shock'. *J. Geophys. Res.* **109**, A05207, doi: 10.1029/2003JA010056.

Anderson, B., S. A. Fuselier, S. P. Gary, and R. E. Denton: 1994, 'Magnetic spectral signatures in the Earth's magnetosheath and plasma depletion layer'. *J. Geophys. Res.* **99**, 5877–5891.

Armstrong, T. P., M. E. Pesses, and R. B. Decker: 1985, 'Shock drift acceleration'. In: B. T. Tsurutani and R. G. Stone (eds.): *Collisionless shocks in the heliosphere: reviews of current research*, AGU Monograph Series 35. Washington, D.C.: Amer. Geophys. Union, pp. 271–285.

Balikhin, M. A. and M. E. Gedalin: 1993, 'Comparative analysis of different methods for distinguishing temporal and spatial variations'. In: *Proc. of START Conf., Aussois, France*, Vol. ESA WPP 047. pp. 183–187.

Balikhin, M. A., O. A. Pokhotelov, S. N. Walker, E. Amata, M. Andre, M. Dunlop, and H. S. K. Alleyne: 2003, 'Minimum variance free wave identification: Application to Cluster electric field data in the magnetosheath'. *Geophys. Res. Lett.* **30**(10), 1508, doi:10.1029/2003GL016918.

Balogh, A., C. M. Carr, M. H. Acuña, M. W. Dunlop, T. J. Beek, P. Brown, K.-H. Fornaçon, E. Georgescu, K.-H. Glassmeier, J. Harris, G. Musmann, T. Oddy, and K. Schwingenschuh: 2001, 'The Cluster Magnetic Field Investigation: overview of in-flight performance and initial results'. *Ann. Geophys.* **19**, 1207–1217.

Baumjohann, W. and R. A. Treumann: 1996, *Basic space plasma physics*. London: Imperial College Press.

Baumjohann, W., R. A. Treumann, E. Georgescu, G. Haerendel, K.-H. Fornaçon, and U. Auster: 1999, 'Waveform and packet structure of lion roars'. *Ann. Geophys.* **17**, 1528–1534.

Bell, A. R.: 1978, 'The acceleration of cosmic rays in shock fronts'. *Mon. Not. R. Astron. Soc.* **182**, 147–156 and 443–455.

Bernstein, I. B., J. M. Greene, and M. D. Kruskal: 1957, 'Exact nonlinear plasma oscillations'. *Phys. Rev.* **108**, 546–550.

Brinca, A. L., N. Sckopke, and G. Paschmann: 1990, 'Wave excitation downstream of the low-beta, quasi-perpendicular bow shock'. *J. Geophys. Res.* **95**, 6331–6335.

Cattell, C., C. Neiman, J. Dombeck, J. Crumley, J. Wygant, C. A. Kletzing, W. K. Peterson, F. S. Mozer, and M. Andre: 2003, 'Large amplitude solitary waves in and near Earth's magnetosphere, magnetopause and bow shock: Polar and Cluster observations'. *Nonlinear Proc. Geophys.* **10**, 13–26.

Chandrasekhar, S., A. N. Kaufman, and K. M. Watson: 1958, 'The stability of the pinch'. *Proc. R. Soc. London, Ser. A* **245**, 435–455.

Chen, L.-J., D. J. Thouless, and J.-M. Tang: 2004, 'Bernstein-Greene-Kruskal solitary waves in three-dimensional magnetized plasma'. *Phys. Rev. E* **69**, 055401–1–055401–4.

Chisham, G., D. Burgess, S. J. Schwartz, and M. W. Dunlop: 1998, 'Observations of electron distributions in magnetosheath mirror mode waves'. *J. Geophys. Res.* **103**, 26765–26774.

Constantinescu, O. D.: 2002, 'Self-consistent model for mirror structures'. *J. Atmos. Terr. Phys.* **64**, 645–649.

Constantinescu, O. D., K.-H. Glassmeier, R. Treumann, and K.-H. Fornaçon: 2003, 'Magnetic mirror structures observed by Cluster in the magnetosheath'. *Geophys. Res. Lett.* **30**, 1802, doi:10.1029/2003GL017313.

Cornilleau-Wehrlin, N., G. Chanteur, S. Perraut, L. Rezeau, P. Robert, A. Roux, C. Villedary, P. Canu, M. Maksimovic, Y. Conchy, D. Lacombe, F. Lefeuvre, M. Parrot, J. Pinçon, P. Décréau, C. Harvey, P. Louarn, O. Santolík, H. Alleyne, M. Roth, T. Chust, O. Contel, and The Staff Investigator Team: 2003, ' First results obtained by the Cluster STAFF experiment '. *Ann. Geophys.* **21**, 437–456.

Cornilleau-Wehrlin, N., P. Chauveau, S. Louis, A. Meyer, J. M. Nappa, S. Perraut, R. L., P. Robert, A. Roux, C. De Villedary, Y. De Conchy, L. Friel, C. C. Harvey, D. Hubert, C. Lacombe, R. Manning, F. Wouters, F. Lefeuvre, M. Parrot, J. L. Pincon, B. Poirier, W. Kofman, P. Louarn, and The Staff Investigator Team: 1997, 'The Cluster Spatio-Temporal Analysis of Field Fluctuations (STAFF) Experiment'. *Space Sci. Rev.*. **79**, 107–136.

Crooker, N. U. and G. L. Siscoe: 1977, 'A mechanism for pressure anisotropy and mirror instability in the dayside magnetosheath'. *J. Geophys. Res.* **82**, 185–186.

Denton, R. E., S. P. Gary, B. Anderson, S. A. Fuselier, and M. K. Hudson: 1994, 'Low frequency magnetic spectra in the magnetosheath and plasma depletion layer'. *J. Geophys. Res.* **99**, 5893–5901.

Denton, R. E., S. P. Gary, X. Li, B. J. Anderson, J. W. Labelle, and M. Lessard: 1995, 'Low-frequency fluctuations in the magnetosheath near the magnetopause'. *J. Geophys. Res.* **100**, 5665–5679.

Dubouloz, N., R. A. Treumann, R. Pottelette, and M. Malingre: 1993, 'Turbulence generated by a gas of electron acoustic solitons'. *J. Geophys. Res.* **98**(A10), 17415–17422, 10.1029/93JA01611.

Dudok de Wit, T., V. V. Krasnosel'skikh, S. D. Bale, M. W. Dunlop, H. Lühr, S. J. Schwartz, and L. J. C. Woolliscroft: 1995, 'Determination of dispersion relations in quasi-stationary plasma turbulence using dual satellite data'. *Geophys. Res. Lett.* **22**, 2653–2656.

Eastwood, J., E. A. Lucek, C. Mazelle, K. Meziane, Y. Narita, J. Pickett, R. Treumann, and P. Décréau: 2005, 'The Foreshock'. *Space Sci. Rev.* **this issue**.

Ergun, R. E., C. W. Carlson, J. P. McFadden, F. S. Mozer, G. T. Delory, W. Peria, C. Chaston, M. Temerin, I. Roth, I. Muschietti, R. Elphic, R. Strangeway, R. Pfaff, C. A. Cattell, D. Klumpar, E. Shelley, W. Peterson, E. Moebius, and L. Kistler: 1998, 'FAST satellite observations of large amplitude solitary structures'. *Geophys Res. Lett.* **25**, 2041–2044.

Franz, J. A., P. M. Kintner, and J. S. Pickett: 1998, 'POLAR observations of coherent electric field structures'. *Geophys. Res. Lett.* **25**, 1277–1280.

Gary, S. P., P. D. Convery, R. E. Denton, S. A. Fuselier, and B. J. Anderson: 1994, 'Proton and helium cyclotron anisotropy instability thresholds in the magnetosheath'. *J. Geophys. Res.* **99**, 5915–5921.

Glassmeier, K.-H., U. Motschmann, M. Dunlop, A. Balogh, M. H. Acuña, C. Carr, G. Musmann, K.-H. Fornaçon, K. Schweda, J. Vogt, E. Georgescu, and S. Buchert: 2001, 'Cluster as a wave telescope - first results from the fluxgate magnetometer'. *Ann. Geophys.* **19**, 1439–1447.

Gleaves, D. G. and D. J. Southwood: 1991, 'Magnetohydrodynamic fluctuations in the earth's magnetosheath at 1500 LT - ISEE 1 and ISEE 2'. *J. Geophys. Res.* **96**, 129–142.

Goldstein, B. E., E. J. Smith, A. Balogh, T. S. Horbury, M. L. Goldstein, and D. A. Roberts: 1995, 'Properties of magnetohydrodynamic turbulence in the solar wind as observed by Ulysses at high heliographic latitudes'. *Geophys. Res. Lett.* **22**, 3393–3396.

Gurnett, D. A., L. A. Frank, and R. P. Lepping: 1976, 'Plasma waves in the distant magnetotail'. *J. Geophys. Res.* **81**, 6059–6071.

Gurnett, D. A., R. L. Huff, and D. L. Kirchner: 1997, 'The Wide-Band Plasma Wave Investigation'. *Space Sci. Rev.* **79**, 195–208.

Gustafsson, G., R. Bostrom, B. Holback, G. Holmgren, A. Lundgren, K. Stasiewicz, L. Ahlen, F. S. Mozer, D. Pankow, P. Harvey, P. Berg, R. Ulrich, A. Pedersen, R. Schmidt, A. Butler, A. W. C. Fransen, D. Klinge, C.-G. Falthammar, P.-A. Lindqvist, S. Christenson, J. Holtet, B. Lybekk, T. A. Sten, P. Tanskanen, K. Lappalainen, and J. Wygant: 1997, 'The Electric Field and Wave Experiment for the Cluster mission'. *Space Sci. Rev.* **79**, 137–156.

Hasegawa, A.: 1969, 'Drift mirror instability in the magnetosphere'. *Phys. Fluids* **12**, 2642–2650.

Hill, P., G. Paschmann, R. A. Treumann, W. Baumjohann, N. Sckopke, and H. Lühr: 1995, 'Plasma and magnetic field behavior across the magnetosheath near local noon'. *J. Geophys. Res.* **100**, 9575–9584.

Horbury, T. S. and A. Balogh: 1997, 'Structure function measurements of the intermittent MHD turbulent cascade'. *Nonlinear Proc. Geophys.* **4**, 185–199.

Horbury, T. S., A. Balogh, R. J. Forsyth, and E. J. Smith: 1995, 'Observation of evolving turbulence in the polar solar wind'. *Geophys. Res. Lett.* **22**, 3401–3404.

Horbury, T. S., E. A. Lucek, A. Balogh, I. Dandouras, and H. Rème: 2004, 'Motion and orientation of magnetic field dips and peaks in the terrestrial magnetosheath'. *J. Geophys. Res.* **109**(A18), doi:10.1026/2003JA0101237.

Kivelson, M. G. and C. T. Russell: 1995, *Introduction to space physics*. Cambridge ; New York : Cambridge University Press, 1995.

Kivelson, M. G. and D. J. Southwood: 1996, 'Mirror instability. II - The mechanism of nonlinearsaturation'. *J. Geophys. Res.* **101**, 17365–17371.

Lacombe, C., G. Belmont, D. Hubert, C. C. Harvey, A. Mangeney, C. T. Russell, J. T. Gosling, and S. A. Fuselier: 1995, 'Density and magnetic field fluctuations observed by ISEE 1-2 in the quiet magnetosheath'. *Ann. Geophys.* **13**, 343–357.

Laveder, D., T. Passot, and P. L. Sulem: 2002, 'Transverse dynamics of dispersive Alfvén waves: Direct numerical evidence of filamentation'. *Phys. Plasmas* **9**, 293–304.

Lee, L. C., C. S. Wu, and C. P. Price: 1987, 'On the generation of magnetosheath lion roars'. *J. Geophys. Res.* **92**, 2343–2348.

Li, X., H. R. Lewis, J. Labelle, T.-D. Phan, and R. A. Treumann: 1995, 'Characteristics of the ion pressure tensor in the Earth's magnetosheath'. *Geophys. Res. Lett.* **22**, 667–670.

Louarn, P., E. Budnik, J. A. Sauvaud, G. Parks, K. Meziane, J. M. Bosqued, I. Dandouras, H. Rème, U. Mall, P. Daly, M. Dunlop, A. Balogh, L. M. Kistler, and E. Amata: 2003, 'Observations of energy-time dispersed ion signatures in the magnetosheath by CLUSTER: possible signatures of transient acceleration processes at the shock'. *Ann. Geophys.* **21**, 1483–1495.

Lucek, E. A., M. W. Dunlop, A. Balogh, P. Cargill, W. Baumjohann, E. Georgescu, G. Haerendel, and K. H. Fornaçon: 1999, 'Identification of magnetosheath mirror modes in Equator-S magnetic field data'. *Ann. Geophys.* **17**, 1560–1573.

Lucek, E. A., M. W. Dunlop, T. S. Horbury, A. Balogh, P. Brown, P. Cargill, C. Carr, K. H. Fornacon, E. Georgescu, and T. Oddy: 2001, 'Cluster magnetic field observations in the magnetosheath: four-point measurements of mirror structures'. *Ann. Geophys.* **19**, 1421–1428.

Maksimovic, M., S. D. Bale, T. S. Horbury, and M. Andre: 2003, 'Bow shock motions observed with Cluster '. *Geophys. Res. Lett.* **30**, 1393, doi:10.1029/2002GL016761.

Maksimovic, M., C. C. Harvey, O. Santolik, C. Lacombe, Y. de Conchy, D. Hubert, P. F., N. Cornilleau-Werhlin, I. Dandouras, E. A. Lucek, and A. Balogh: 2001, 'Polarisation and propagation of Lion Roars in the dusk side Magnetosheath'. *Ann. Geophys.* **19**, 1429–1438.

Mangeney, C., C. Salem, C. Lacombe, J.-L. Bougeret, C. Perche, R. Manning, P.-J. Kellogg, K. Goetz, J. Monson, and J.-M. Bosqued: 1999, 'WIND observations of coherent electrostatic waves in the solar wind'. *Ann. Geophys.* **17**, 307–320.

Marsch, E. and C.-Y. Tu: 1997, 'Intermittency, non-Gaussian statistics and fractal scaling of MHD fluctuations in the solar wind'. *Nonlin. Proc. Geophys.* **4**, 101–124.

Matsumoto, H., H. Kojima, T. Miyatake, Y. Omura, M. Okada, I. Nagano, and M. Tsutsui: 1994, 'Electrostatic solitary waves (ESW) in the magnetotail: BEN wave forms observed by GEOTAIL'. *Geophys. Res. Lett.* **21**, 2915–2918.

Matthaeus, W. H., M. L. Goldstein, and D. A. Roberts: 1990, 'Evidence for the presence of quasi-two-dimensional nearly incompressible fluctuations in the solar wind'. *J. Geophys. Res.* **91**, 20673–20683.

Means, J. D.: 1972, 'Use of the three-dimensional covariance matrix in analyzing the polarization properties of plane waves'. *J. Geophys. Res.* **77**, 5551–5559.

Motschmann, U., K.-H. Glassmeier, and J. L. Pinçon: 1998, 'Plasma mode recognition'. In: G. Paschmann and P. W. Daly (eds.): *Analysis Methods for Multi-Spacecraft Data*, ISSI SR-001. ESA Publications Division, pp. 79–89.

Motschmann, U., T. I. Woodward, K.-H. Glassmeier, D. J. Southwood, and J. L. Pinçon: 1996, 'Wavelength and direction filtering by magnetic measurements at satellite arrays: Generalized minimum variance analysis'. *J. Geophys. Res.* **101**, 4961–4965.

Omidi, N., A. O'Farrell, and D. Krauss-Varban: 1994, 'Sources of magnetosheath waves and turbulence'. *Adv Space Res.* **14**, 745–754.

Pantellini, F. G. E. and S. J. Schwartz: 1995, 'Electron temperature effects in the linear proton mirrorinstability'. *J. Geophys. Res.* **100**, 3539–3549.

Paschmann, G., G. Haerendel, N. Sckopke, E. Möbius, H. Lühr, and C. W. Carlson: 1988, 'Three-dimensional plasma structures with anomalous flow directions near the Earth's bow shock'. *J. Geophys. Res.* **93**, 11279–11294.

Paschmann, G., N. Sckopke, J. R. Asbridge, S. J. Bame, and J. T. Gosling: 1980, 'Energization of solar wind ions by reflection from the earth's bow shock'. *J. Geophys. Res.* **85**, 4689–4693.

Paschmann, G., N. Sckopke, I. Papamastorakis, J. R. Asbridge, S. J. Bame, and J. T. Gosling: 1981, 'Characteristics of reflected and diffuse ions upstream from the Earth's bow shock'. *J. Geophys. Res.* **86**, 4355–4364.

Phan, T. D., D. Larson, J. McFadden, R. P. Lin, C. Carlson, M. Moyer, K. I. Paularena, M. McCarthy, G. K. Parks, H. Rème, T. R. Sanderson, and R. P. Lepping: 1997, 'Low-latitude dusk flank magnetosheath, magnetopause, and boundary layer for low magnetic shear: Wind observations'. *J. Geophys. Res.* **102**, 19883–19896.

Phan, T. D., D. E. Larson, R. P. Lin, J. P. McFadden, K. A. Anderson, C. W. Carlson, R. E. Ergun, S. M. Ashford, M. P. McCarthy, G. K. Parks, H. . Reme, J. M. Bosqued, C. D'Uston, K.-P. Wenzel, T. R. Sanderson, and A. Szabo: 1996, 'The subsolar magnetosheath and magnetopause for high solar wind ram pressure: WIND observations'. *Geophys. Res. Lett.* **23**, 1279.

Phan, T.-D., G. Paschmann, W. Baumjohann, N. Sckopke, and H. Lühr: 1994, 'The magnetosheath region adjacent to the dayside magnetopause: AMPTE/IRM observations'. *J. Geophys. Res.* **99**, 121–141.

Pickett, J. S., L.-J. Chen, S. W. Kahler, O. Santolik, D. A. Gurnett, B. T. Tsurutani, and A. Balogh: 2004a, 'Isolated electrostatic structures observed through the Cluster orbit: Relationship to magnetic field strength'. *Ann. Geophys.* **22**, 2515–2523.

Pickett, J. S., S. W. Kahler, L.-J. Chen, R. L. Huff, O. Santolik, Y. Khotyaintsev, P. M. E. Decreau, D. Winningham, R. Frahm, M. L. Goldstein, G. S. Lakhina, B. T. Tsurutani, B. Lavraud, D. A. Gurnett, A. Andre, A. Fazakerley, A. Balogh, and H. Reme: 2004b, 'Solitary waves observed in the auroral zone: the Cluster multi-spacecraft perspective'. *Nonlinear Proc. Geophys.* **1**, 1–14.

Pickett, J. S., J. D. Menietti, D. A. Gurnett, B. Tsurutani, P. M. Kintner, E. Klatt, and A. Balogh: 2003, 'Solitary potential structures observed in the magnetosheath by the Cluster spacecraft'. *Nonlinear Proc. Geophys.* **11**, 183–196.

Pinçon, J. and F. Lefeuvre: 1991, 'Local characterization of homogeneous turbulence in a space plasma from simultaneous measurement of field components at several points in space'. *J. Geophys. Res.* **96**, 1789–1802.

Pinçon, J. and U. Motschmann: 1998, 'Multi-Spacecraft Filtering: General Framework'. In: G. Paschmann and P. Daly (eds.): *Analysis methods for multi-spacecraft data*, ISSI Sci. Rep. SR-001. Bern: ISSI, pp. 65–78.

Pokhotelov, O. A., M. A. Balikhin, R. A. Treumann, and V. P. Pavlenko: 2001, 'Drift mirror instability revisited: 1. Cold electron temperature limit'. *J. Geophys. Res.* **106**, 8455–8464.

Pokhotelov, O. A. and V. A. Pilipenko: 1976, 'Contribution to the theory of the drift-mirror instability of the magnetospheric plasma'. *Geomagnetizm i Aeronomiia* **16**, 504–510.

Pokhotelov, O. A., R. Z. Sagdeev, M. A. Balikhin, and R. A. Treumann: 2004, 'The mirror instability at finite ion-Larmor radius wavelengths'. *J. Geophys. Res.* **109**, A09213, doi:10.1029/2004JA010568.

Pokhotelov, O. A., I. Sandberg, R. Z. Sagdeev, R. A. Treumann, O. G. Onishchenko, M. A. Balikhin, and V. P. Pavlenko: 2003, 'Slow drift mirror modes in finite electron-temperature plasma: Hydrodynamic and kinetic drift mirror instabilities'. *J. Geophys. Res.* **108**, 1098, doi:10.1029/2002JA009651.

Rème, H., C. Aoustin, J. M. Bosqued, I. Dandouras, B. Lavraud, J. A. Sauvaud, A. Barthe, J. Bouyssou, T. Camus, O. Coeur-Joly, A. Cros, J. Cuvilo, F. Ducay, Y. Garbarowitz, J. L. Medale, E. Penou, H. Perrier, D. Romefort, J. Rouzaud, C. Vallat, D. Alcaydé, C. Jacquey, C. Mazelle, C. Uston, E. Möbius, L. M. Kistler, K. Crocker, M. Granoff, C. Mouikis, M. Popecki, M. Vosbury, B. Klecker, D. Hovestadt, H. Kucharek, E. Kuenneth, G. Paschmann, M. Scholer, N. Sckopke, E. Seidenschwang, C. W. Carlson, D. W. Curtis, C. Ingraham, R. P. Lin, J. P. McFadden, G. K. Parks, T. Phan, V. Formisano, E. Amata, M. B. Bavassano-Cattaneo, P. Baldetti, R. Bruno, G. Chionchio, A. D. Lellis, M. F. Marcucci, G. Pallocchia, A. Korth, P. W. Daly, B. Graeve, H. Rosenbauer, V. Vasyliunas, M. McCarthy, M. Wilber, L. Eliasson, R. Lundin, S. Olsen, E. G. Shelley, S. Fuselier, A. G. Ghielmetti, W. Lennartsson, C. P. Escoubet, H. Balsiger, R. Friedel, J.-B. Cao, R. A. Kovrazhkin, I. Papamastorakis, R. Pellat, J. Scudder, and B. Sonnerup: 2001, 'First multispacecraft ion measurements in and near the Earth's magnetosphere with the identical Cluster Ion Spectrometry (CIS) experiment'. *Ann. Geophys.* **19**, 1303–1354.

Robert, P., A. Roux, C. C. Harvey, M. W. Dunlop, P. W. Daly, and K.-H. Glassmeier: 1998, 'Tetrahedron geometric factors'. In: G. Paschmann and P. W. Daly (eds.): *Analysis Methods for Multi-Spacecraft Data*, ISSI SR-001. ESA Publications Division, pp. 332–348.

Roberts, D. A. and M. L. Goldstein: 1991, 'Turbulence and waves in the solar wind'. *Rev. Geophys., Suppl.* **29**, 932–943.

Rodriguez, P.: 1979, 'Magnetosheath electrostatic turbulence'. *J. Geophys. Res.* **84**, 917–930.

Rodriguez, P.: 1985, 'Magnetosheath whistler turbulence'. *J. Geophys. Res.* **90**, 6337–6342.

Roelof, E. C. and D. C. Sibeck: 1993, 'Magnetopause shape as a bivariate function of interplanetary magnetic field b_z and solar wind dynamic pressure'. *J. Geophys. Res.* **98**, 21421–21450.

Rönnmark, K.: 1983, 'Computation of the dielectric tensor of a Maxwellian plasma'. *Plasma Phys.* **25**, 699–701.

Rudakov, L. I. and R. Z. Sagdeev: 1959, 'A quasi-hydrodynamic description of a rarefied plasma in a magnetic field'. *Plasma Physics and the problem of controlled thermonuclear reactions* **3**, 321–335.

Safránková, J., L. Prech, Z. Nemecek, D. G. Sibeck, and T. Mukai: 2000, 'Magnetosheath response to the interplanetary magnetic field tangential discontinuity'. *J. Geophys. Res.* **105**, 25113–25121.

Sahraoui, F., J. L. Pinçon, G. Belmont, L. Rezeau, N. Cornilleau-Wehrlin, P. Robrt, L. Mellul, J. M. Bosqued, A. Balogh, P. Canu, and G. Chanteur: 2003, 'ULF wave identification in the magnetosheath: The k-filtering technique applied to Cluster II data'. *J. Geophys. Res.* **108**, 1335, doi:10.1029/2002JA009587.

Santolik, O. and D. A. Gurnett: 2003, 'Transverse dimensions of chorus in the source region'. *Geophys. Res. Lett.* **30**, 1031, doi:10.1029/2002GL016178.

Scarf, F. L., L. A. Frank, K. L. Ackerson, and R. P. Lepping: 1974, 'Plasma wave turbulence at distant crossings of the plasma sheet boundaries and the neutral sheet'. *Geophys. Res. Lett.* **1**, 189–192.

Schwartz, S. J., D. Burgess, and J. J. Moses: 1996, 'Low frequency waves in the Earth's magnetosheath: Present status'. *Ann. Geophys.* **14**, 1134–1150.

Schwartz, S. J., R. L. Kessel, C. C. Brown, L. J. C. Woolliscroft, M. W. Dunlop, C. J. Farrugia, and D. S. Hall: 1988, 'Active current sheets near the Earth's bow shock'. *J. Geophys. Res.* **93**, 11295–11310.

Sckopke, N., G. Paschmann, S. J. Bame, J. T. Gosling, and C. T. Russell: 1983, 'Evolution of ion distributions across the nearly perpendicular bow shock - Specularly and non-specularly reflected-gyrating ions'. *J. Geophys. Res.* **88**, 6121–6136.

Sckopke, N., G. Paschmann, A. L. Brinca, C. W. Carlson, and H. Lühr: 1990, 'Ion thermalization in quasi-perpendicular shocks involving reflected ions'. *J. Geophys. Res.* **95**, 6337–6352.

Sibeck, D. G., N. L. Borodkova, S. J. Schwartz, C. J. Owen, R. Kessel, S. Kokubun, R. P. Lepping, R. Lin, K. Liou, H. Lühr, R. W. McEntire, C.-I. Meng, T. Mukai, Z. Nemecek, G. Parks, T. D. Phan, S. A. Romanov, J. Safrankova, J.-A. Sauvaud, H. J. Singer, S. I. Solovyev, A. Szabo, K. Takahashi, D. J. Williams, K. Yumoto, and G. N. Zastenker: 1999, 'Comprehensive study of the magnetospheric response to a hot flow anomaly'. *J. Geophys. Res.* **104**, 4577–4593.

Sibeck, D. G., N. L. Borodkova, G. N. Zastenker, S. A. Romanov, and J.-A. Sauvaud: 1998, 'Gross deformation of the dayside magnetopause'. *Geophys. Res. Lett.* **25**, 453–456.

Smith, E. J., R. E. Holzer, M. G. McLeon, and C. T. Russell: 1967, 'Magnetic noise in the magnetosheath in the frequency range 3-300 Hz'. *J. Geophys. Res.* **72**, 4803–4813.

Smith, E. J. and B. T. Tsurutani: 1976, 'Magnetosheath lion roars'. *J. Geophys. Res.* **81**, 2261–2266.

Song, P., C. T. Russell, and S. P. Gary: 1994, 'Identification of low-frequency fluctuations in the terrestrial magnetosheath'. *J. Geophys. Res.* **99**, 6011–6025.

Song, P., C. T. Russell, and M. F. Thomsen: 1992, 'Waves in the inner magnetosheath: a case study'. *Geophys. Res. Lett.* **19**, 2191–2194.

Stasiewicz, K.: 2004, 'Theory and observations of slow-mode solitons in space plasmas'. *Physical Review Letters* **93**(12), 125004.

Tajiri, M.: 1967, 'Propagation of hydromagnetic waves in collisionless plasma II, Kinetic approach'. *J. Phys. Soc. Jpn.* **22**, 1482–1498.

Treumann, R. A. and W. Baumjohann: 1997, *Advanced space plasma physics*. London : Imperial College Press, 1997.

Treumann, R. A., E. Georgescu, and W. Baumjohann: 2000, 'Lion roar trapping in mirror modes'. *Geophys. Res. Lett.* **27**, 1843–1846.

Treumann, R. A., C. H. Jaroschek, O. D. Constantinescu, R. Nakamura, O. A. Pokhotelov, and E. Georgescu: 2004, 'The strange physics of low frequency mirror mode turbulence in the high temperature plasma of the magnetosheath'. *Nonlin. Proc. Geophys.* **11**, 647–657.

Tsurutani, B. T., E. J. Smith, R. R. Anderson, K. W. Ogilvie, J. D. Scudder, D. N. Baker, and S. J. Bame: 1982, 'Lion roars and nonoscillatory drift mirror waves in the magnetosheth'. *J. Geophys. Res.* **87**, 6060–6072.

Tu, C.-Y. and E. Marsch: 1995, 'MHD structures, waves and turbulence in the solar wind: Obsevations and theories'. *Space Sci. Rev.* **73**, 1–210.

Walker, S. N., F. Sahraoui, M. A. Balikhin, G. Belmont, J. L. Pinçon, L. Rezeau, H. Alleyne, N. Cornilleau-Wehrlin, and M. André: 2004, 'A Comparison of Wave Mode identification Techniques'. *Ann. Geophys.* **22**, 3021–3032.

Zhang, Y., H. Matsumoto, and H. Kojima: 1998, 'Lion roars in the magnetosheath: the Geotail observations'. *J. Geophys. Res.* **103**, 4615–4626.